Cross-Correlated Relaxation in the NMR of Near-Equivalent Spin Pairs: Longitudinal Relaxation and Long-lived Singlet Order

James W. Whipham, Mohamed Sabba, Gamal Moustafa, and Malcolm H. Levitt
School of Chemistry, Southampton University, SO17 1BJ, UK

Laurynas Dagys
School of Chemistry, Southampton University, SO17 1BJ, UK and
Institute of Chemical Physics, Vilnius University, LT-10257, Lithuania

Christian Bengs
School of Chemistry, Southampton University, SO17 1BJ, UK and
Department of Chemistry, University of California, Berkeley CA 94720, USA

(Dated: May 30, 2024)

The evolution of nuclear spin state populations is investigated for the case of a $^{13}C_2$-labelled triyne in solution, for which the near-equivalent coupled pairs of ^{13}C nuclei experience cross-correlated relaxation mechanisms. Inversion-recovery experiments reveal different recovery curves for the main peak amplitudes, especially when the conversion of population imbalances to observable coherences is induced by a radiofrequency pulse with a small flip angle. Measurements are performed over a range of magnetic fields by using a sample shuttle apparatus. In some cases, the time constant T_S for decay of nuclear singlet order is more than 100 times larger than the time constant T_1 for equilibration of longitudinal magnetization. The results are interpreted by a theoretical model incorporating cross-correlated relaxation mechanisms, anisotropic rotational diffusion, and an external random magnetic field. A Lindbladian formalism is used to describe the dissipative dynamics of the spin system in an environment of finite temperature. Good agreement is achieved between theory and experiment.

I. INTRODUCTION

In our previous paper [1], we explored the effects of cross-correlated relaxation on the NMR lineshapes of strongly coupled ^{13}C pairs in the near-equivalence regime. The molecular system under study, denoted here as **I**, is shown in figure 1. This is a $^{13}C_2$-labelled triyne, with two different end groups creating a small difference in isotropic chemical shifts between the two ^{13}C sites. Since the resonance frequency difference between the two ^{13}C sites is much smaller than the J-coupling between the ^{13}C nuclei, each $^{13}C_2$ pair forms a near-equivalent AB system in isotropic solution [2]. Three of the four energy eigenstates of the ^{13}C pair are given, to a good approximation, by the three components of the spin-1 triplet state of the spin pair, while the remaining state is approximately equal to the spin-0 singlet state [2]. The rod-like shape of **I** causes strongly anisotropic rotational diffusion in solution [1].

FIG. 1. Schematic representation of **I**, with black circles representing ^{13}C labels. The different substituents at the ends of the molecule give a small chemical shift difference of 0.16 ppm between the two ^{13}C sites.

As shown in ref. [1], the ^{13}C NMR spectrum consists of four peaks, with two strong central peaks associated with single-quantum coherences between the near-triplet states, and two weak outer peaks associated with coherences between the near-singlet state and the outer near-triplet states. A large difference in the NMR linewidths is observed for the two triplet-triplet peaks, and is attributed to strong correlation between the fluctuating chemical shift anisotropy and dipole-dipole coupling interactions [3–10]. Reference [1] gives explicit analytical expressions, under some approximations, for the positions and linewidths of the spectral peaks, in the presence of cross-correlated relaxation driven by anisotropic rotational diffusion. Good agreement with experiment was achieved.

In this paper, we continue our investigations of the NMR relaxation of **I** in isotropic solution. In the current paper, we consider the relaxation of the spin state populations, as investigated by inversion-recovery NMR experiments. As shown below, inversion-recovery NMR experiments display a strong asymmetry between the recovery trajectories of the different spectral peaks after an initial pulse. The asymmetry in the recovery to thermal equilibrium is associated with the cross-correlation of the chemical shift anisotropy and dipole-dipole interactions [5, 8, 11–14].

We also present the results of NMR experiments which demonstrate the long decay time constant T_S of $^{13}C_2$ singlet order for **I** in solution, where the term singlet order means the population imbalance between the singlet state and the triplet manifold [15–18]. The singlet decay time constant T_S is found to exceed the magnetization relaxation time constant T_1 by a factor of more than 100

under some conditions. The slow decay of nuclear singlet order is due, in this case, to the strong cross-correlation of the chemical shift anisotropy interactions for the two ^{13}C sites, as well as the immunity of singlet order to relaxation caused by dipole-dipole interactions within the spin pair.

Since the phenomena of interest involve the approach of nuclear spin systems to thermal equilibrium, the associated relaxation theory must take into account the finite temperature of the thermal environment. There are several methods for introducing the finite environmental temperature into standard NMR relaxation theories, which is based on second-order perturbation theory, as formulated by Bloch, Wangsness, Redfield and Abragam [19–21]. The prevalent method, used for example in the books by Abragam [21] and Ernst *et al.* [22] is to introduce the thermal equilibrium density operator $\rho_{\rm eq}$ as an *ad hoc* correction to the Liouville-von Neumann equation. This leads to the inhomogeneous master equation (IME) [22]. However, this equation provides, in some circumstances, incorrect and even physically impossible predictions [23, 24]. In the current work, we use instead a Lindbladian formulation of the relaxation superoperator which is consistent with the rigorous theory of open quantum systems [23–27]. The resulting theory accurately predicts analytical operator trajectories and peak amplitudes, which in turn offer physically intuitive insight into the population dynamics throughout the relaxation process.

II. METHODS

A. Sample

Experiments were performed on the $^{13}C_2$-labelled triyne derivative shown in figure 1, and referred to as **I**. The synthesis of **I** is given in the supplementary information of our previous article [1]. The sample consisted of 19 mg of **I**, made up to a 200 μL 0.3 M solution in $CDCl_3$. The solution was degassed by 5 freeze-thaw cycles.

B. Equipment

All high-field experiments were performed on a 400 MHz (9.4 T) Bruker Avance Neo spectrometer. For the low-field experiments, the sample was mechanically transported from the bore of the spectrometer to a position above the magnet.

The custom-built sample shuttle was based on a design by Kiryutin [28, 29], in which the sample shuttle was mounted above the spectrometer, and the sample is mechanically transported to a region of low field. The sample is mounted on a carriage and transported on a rail system via control by a stepper motor, which in turn is controlled by the spectrometer pulse program. In our shuttle system, the sample is at high field (9.4 T) prior to shuttling. The shuttling to low field takes approximately 0.25 s.

C. Pulse Sequences

In all experiments the ^{13}C radiofrequency field corresponded to a nutation frequency of 29.4 kHz. The NMR signal was sampled with 128 k data points with a spectral width of 81.46 ppm.

1. *Variable flip-angle inversion-recovery*

Inversion-recovery experiments were conducted using the pulse sequence shown in figure 2. The equilibrium spin-state populations were inverted by a $90^\circ_y 180^\circ_x 90^\circ_y$ composite pulse [30], followed by a variable delay τ, and excitation of observable transverse magnetization by a read-out pulse of flip-angle β. The NMR signal was acquired in the following interval and Fourier transformed to generate the partially-recovered NMR spectrum.

The process was repeated with a set of delays τ between 0.5 s and 35 s in order to track the recovery of inverted longitudinal magnetization. For low-field relaxation experiments, the sample was shuttled to a field < 9.4 T, and back again, during the delay τ.

Separate experiments were performed with the flip-angle β taking values of 10°, 50°, and 90°. As discussed below, the partially-recovered spectra depend on the value of the read-out flip-angle β.

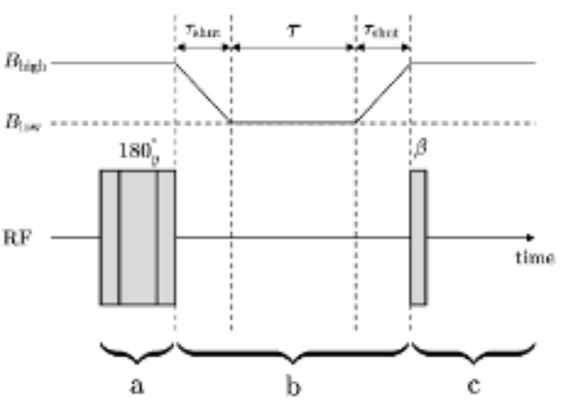

FIG. 2. Pulse sequence for variable flip-angle inversion recovery with optional field cycling. The pulse sequence elements are as follows: (a) 180° composite pulse $90^\circ_y 180^\circ_x 90^\circ_y$ to invert the thermal equilibrium populations. (b) Optional shuttling of the sample to low field over an interval $\tau_{\rm shut} \simeq 0.25$ s, followed by free evolution for a variable interval τ, and shuttling of the sample back to high field over a second interval $\tau_{\rm shut} \simeq 0.25$ s. (c) A pulse with flip angle β creates measurable coherences before acquisition of the signal. The experiments are repeated with the evolution interval τ taking values between 0.5 s and 35 s.

2. Relaxation of singlet order

The relaxation of singlet order was studied as a function of magnetic field strength by the pulse sequence shown in figure 3.

This consists of: (1) A singlet-order destruction (SOD) filter to remove any residual long-lived singlet order left over from the previous transient [31]; (2) A relaxation delay of 6 s to allow the establishment of thermal equilibrium magnetization. (3) An M2S (magnetization-to-singlet) pulse sequence to generate singlet order from thermal equilibrium magnetization [2]; (4) A T_{00}-filter sequence to remove NMR signals not deriving from singlet order [32]; (5) A variable relaxation delay incorporating optional shuttling from high field to low field, and back again; (6) An S2M (singlet-to-magnetization) sequence for regenerating observable magnetization from singlet order [2]; (7) NMR signal acquisition. The M2S, S2M, T_{00}-filter, and SOD-filter sequences are specified in the supplementary material.

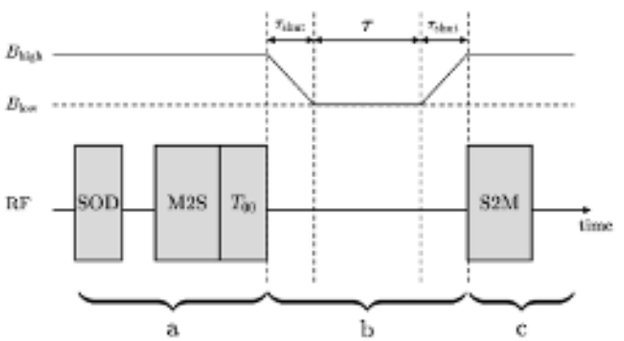

FIG. 3. Pulse sequence used to measure the singlet decay time constant T_S as a function of field strength. a) A singlet order destruction (SOD) filter removes residual singlet order, before thermal equilibrium is established by a 6 s delay, and singlet order is generated by the M2S pulse sequence [2]. A T_{00}-filter removes residual spin order other than singlet order [32]. b) The sample is optionally shuttled to low field in the interval τ_{shut} and evolves freely during the interval τ before being shuttled back to high field in the second τ_{shut} interval. c) Singlet order is converted back to measurable magnetisation via the S2M pulse sequence; i.e. chronological reverse of M2S, with an additional 90° pulse. The NMR signal is detected in the subsequent interval. The evolution interval τ takes values between 0.1 s and 640 s.

III. RESULTS

A. Inversion-Recovery

The results of inversion-recovery experiments are shown in figure 4, for flip angles $\beta = 10°$, 50° and 90°. In each, case a set of spectra is shown, spanning relaxation delays τ between 0.5 s and 35 s. As discussed in our previous paper [1], each spectrum corresponds to a superposition of two Lorentzian peaks with markedly different widths. The asymmetric broadening is due to strong cross-correlation between the dipole-dipole and chemical shift anisotropy relaxation mechanisms [1].

When the flip angle of the last pulse is $\beta = \pi/2 = 90°$ (figure 4, top row), the asymmetric doublet is inverted for small values of τ and then recovers as τ is increased. The two doublet components appear to recover at roughly similar rates, in this case.

The behaviour is distinctly different when the flip angle of the last pulse is small ($\beta = 10°$, figure 4, bottom row). In this case, the right-hand (most shielded) peak clearly recovers much faster than the left-hand (less shielded) peak, and has already partially recovered for the shortest τ delay. The spectral series for $\beta = 50°$ (figure 4, middle row) is intermediate between the two cases.

The peak amplitudes at each value of τ were obtained by fitting each spectrum to a superposition of two absorption Lorentzians as shown in figure 5. The assumed form of the spectral function is,

$$L(\omega) = a_+ \frac{\lambda_+}{\lambda_+^2 + (\omega - \omega_+)^2} + a_- \frac{\lambda_-}{\lambda_-^2 + (\omega - \omega_-)^2}, \quad (1)$$

where $a_\pm$ are the peak amplitudes, $\lambda_\pm$ the linewidths, and $\omega_\pm$ the centre frequencies for the two peaks, as given in our previous article [1].

The centre frequencies $\omega_\pm$ and linewidths $\lambda_\pm$ were determined by fitting a reference spectrum of **I** with the condition $a_+ = a_-$. These frequencies and linewidths were then kept fixed for the analysis of the entire spectral series.

The fitted linewidths are $\lambda_+ = 2\pi \times 0.24\,\text{Hz}$ and $\lambda_- = 2\pi \times 0.34\,\text{Hz}$. The frequency difference between the peaks was estimated to be $|\omega_+ - \omega_-| = 2\pi \times 0.62\,\text{Hz}$. As shown in figure 5, the broader doublet component is shifted to low δ ("high field") relative to the narrower component. This corresponds to $\omega_+ < \omega_-$ when the negative sign of the Larmor frequency is taken into account [33].

The trajectories of the peak amplitudes are shown in figure 6, for the three different flip angles β. These plots clearly show the strong asymmetry between the recovery rates of the two peaks, in the case of a small flip angle β.

In the case of $\beta = \pi/2$, the recovery curve for longitudinal magnetization after inversion is well-described by the function,

$$f(\tau) = a_0\, e^{-\tau/T_1} + a_\infty \left(1 - e^{-\tau/T_1}\right) \quad (2)$$

with a_0 and a_∞ being amplitudes at $\tau = 0$ and $\tau \to \infty$, respectively.

The best-fit T_1 values using eq. (2) are given in table I for fields ranging from 5 mT to 9.39 T. The rate constants T_1^{-1} are plotted as a function of magnetic field in fig. 7a. The T_1^{-1} values between 1.94 and 9.39 T are fitted reasonably well by a field-independent term, which dominates at low field, plus a term that depends on B_0^2,

and which dominates at high field. This quadratic fit is shown by the blue curve in fig. 7a. There is an additional contribution at low magnetic field, the behaviour of which is reminiscent of relaxation induced by dissolved oxygen [34].

B. Singlet Order Relaxation

At all magnetic fields, the integrated signal strength generated by the SOD-M2S-T_{00}-τ-S2M pulse sequence in figure 3 decays monotonically with respect to the waiting interval τ. One example of the slow singlet-order decay is shown in figure 8. For all magnetic fields, the dependence of signal amplitude on τ fits well to a monoexponential decay, of the form:

$$f(\tau) = a_S\, e^{-\tau/T_S}, \tag{3}$$

where a_S is a constant.

The estimated values of T_S are given in table I, which shows that the singlet decay time constant T_S exceeds the magnetization equilibration time constant T_1 by more than a factor of 100, over a wide range of magnetic fields.

The singlet decay rate constant T_S^{-1} is plotted as a function of magnetic field in fig. 7b. The field-dependence of T_S^{-1} is qualitatively similar to that of T_1^{-1}, apart from being ~ 100 times slower. The blue curve in fig. 7b shows a second-order polynomial fitted to the data from 0.845 to 9.4 T. There is an additional contribution at very low field, which may tentatively be ascribed to relaxation induced by paramagnetic dissolved oxygen [17, 34].

TABLE I. Values of T_1 and T_S as a function of static magnetic field strength, from inversion-recovery experiments using $\beta = \pi/2$. The two rows with the largest T_S/T_1 ratios are shown in bold. The rate constants T_1^{-1} and T_S^{-1} are plotted as functions of magnetic field in figure 7.

B_0 / T	T_1 / s	T_S / s	T_S/T_1
9.39	2.2 ± 0.04	209 ± 2	94 ± 2
7.96	2.5 ± 0.1	272 ± 7	111 ± 5
5.11	4.2 ± 0.1	459 ± 15	109 ± 5
1.94	$\mathbf{6.5 \pm 0.2}$	$\mathbf{789 \pm 23}$	$\mathbf{121 \pm 5}$
0.845	$\mathbf{6.2 \pm 0.3}$	$\mathbf{789 \pm 23}$	$\mathbf{127 \pm 7}$
0.409	6.1 ± 0.03	608 ± 14	99 ± 2
0.218	5.9 ± 0.03	509 ± 38	86 ± 6
0.126	5.7 ± 0.2	–	–
0.0428	5.6 ± 0.2	–	–
0.0210	5.8 ± 0.07	–	–
0.0116	5.8 ± 0.03	–	–
0.00695	5.8 ± 0.03	537 ± 50	92 ± 9
0.005	5.5 ± 0.2	549 ± 57	100 ± 11

IV. THEORY

The following theory expands on that given in reference [1], by including the antisymmetric CSA interaction, fluctuating random fields, and a Lindbladian description of the relaxation of the spin system in contact with a finite-temperature environment.

A. Spin Hamiltonian

The spin Hamiltonian consists of coherent and fluctuating terms. Coherent terms are the same for all members of the spin ensemble. Fluctuating stochastic terms differ between the members of spin ensemble and fluctuate randomly in time, causing nuclear spin relaxation.

1. Coherent Hamiltonian

The coherent Hamiltonian may be written,

$$H_{\rm coh} = H_{\rm CS} + H_J, \tag{4}$$

where $H_{\rm CS}$ and H_J are the chemical shift and spin-spin coupling Hamiltonians, respectively. Expressed in a frame rotating about the magnetic field at the mean frequency of the two chemical shifts, these terms take the form,

$$H_{\rm CS} = \frac{1}{2}\omega_\Delta \left(I_{1z} - I_{2z}\right), \tag{5}$$

and,

$$H_J = \omega_J \mathbf{I}_1 \cdot \mathbf{I}_2, \tag{6}$$

with $\omega_\Delta = \omega_0\, \Delta\delta_{\rm iso}$ and $\omega_J = 2\pi J_{\rm iso}$, where ω_0 is the Larmor frequency, $\Delta\delta_{\rm iso}$ is the isotropic chemical shift difference, and $J_{\rm iso}$ is the isotropic spin-spin coupling constant.

For a magnetically equivalent system ($\omega_\Delta = 0$), the eigenbasis of the coherent Hamiltonian consists of the singlet and triplet states [36]. These states span a Hilbert space of dimension $N_{\mathbb{H}} = 4$. For finite ω_Δ, the matrix representation of $H_{\rm coh}$ in this basis is,

$$H_{\rm coh} = \frac{1}{4} \begin{array}{c} \begin{matrix} |S_0\rangle & |T_{+1}\rangle & |T_0\rangle & |T_{-1}\rangle \end{matrix} \\ \begin{pmatrix} -3\omega_J & 0 & 2\omega_\Delta & 0 \\ 0 & \omega_J & 0 & 0 \\ 2\omega_\Delta & 0 & \omega_J & 0 \\ 0 & 0 & 0 & \omega_J \end{pmatrix} \end{array}. \tag{7}$$

The chemical shift frequency difference ω_Δ appears as off-diagonal elements mixing the singlet state $|S_0\rangle$ and the central triplet state $|T_0\rangle$.

2. Fluctuating Hamiltonian

The fluctuating Hamiltonian, which is responsible for the relaxation of the spin system, may be written in the general form,

$$H^\Lambda(t) = c^\Lambda \sum_{\ell=0}^{+2} \sum_{m=-\ell}^{+\ell} (-1)^m A^\Lambda_{\ell-m}(t) X^\Lambda_{\ell m}, \tag{8}$$

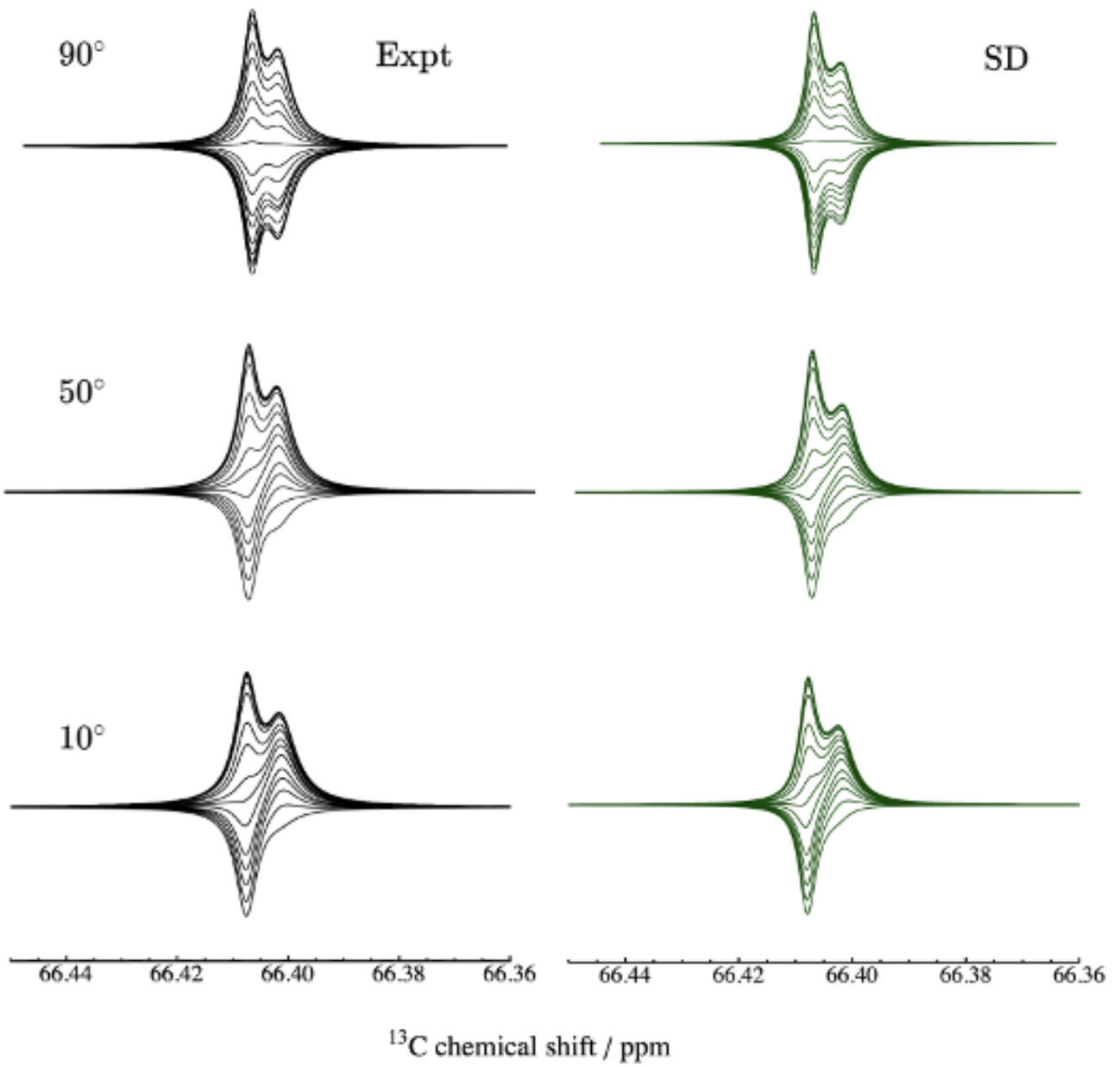

FIG. 4. Left: Experimental inversion-recovery spectra 9.4 T, for $\beta = 10°, 50°, 90°$, obtained by the pulse sequence in figure 2. Spectra are shown for pulse sequence intervals $\tau = \{0.5, 0.75, 1, 1.25, 1.5, 2, 2.5, 3, 4, 5, 7.5, 10, 12.5, 15, 20, 25, 30, 35\}$ s, with the spectra for the shortest interval given by the most negative curves. Right: *SpinDynamica* [35] simulations, using the parameters given in table II.

where c^Λ is a constant for interaction Λ, A^Λ are spatial components of irreducible spherical tensors (IST), and $X^\Lambda_{\ell m}$ are spin, or spin-field, IST operators. The spatial components $A^\Lambda_{\ell m}(t)$ of these interactions fluctuate in time due to the random molecular motion in solution.

In the current molecular system, the most important fluctuating interactions are the dipole-dipole coupling between the two ^{13}C spins and the symmetric components of the two chemical shift anisotropies. These interactions all have spherical rank $\ell = 2$. The terms c^Λ, A^Λ_{2m} and X^Λ_{2m} for these interactions are specified in ref. [1].

The spin-1/2 pair also experiences fluctuating spin-rotation interactions [37, 38], as well as fluctuating sources of magnetic fields located on different molecules. Such intermolecular terms include interactions with nuclear spins on other molecules (including the solvent) and also unpaired electron spins such as dissolved oxygen molecules. For simplicity, we take into account these ad-

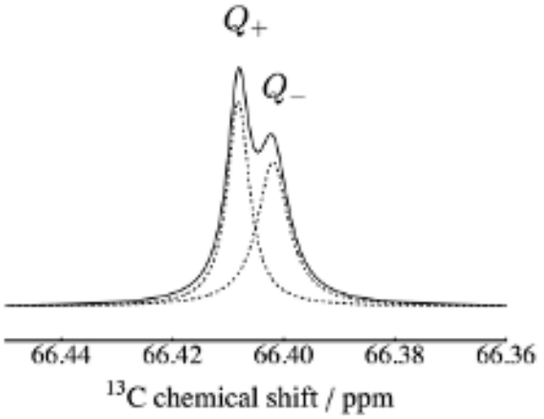

FIG. 5. The 90° pulse-acquire spectrum of a 0.3 M solution of **I** in $CDCl_3$ at 9.39 T fitted as a sum of two absorption Lorentzian functions (eq. (1)). The narrow peak is associated with the single-quantum coherence Q_+, and the broad peak with the coherence Q_-, where the coherence operators $Q_\pm$ are given in equations 46 and 47.

ditional interactions by a simplified model of fluctuating random magnetic fields, as described below.

The coherent and incoherent spin-system parameters assumed for **I** are given in table II.

B. The Liouvillian

The quantum state of the spin ensemble is described by the density operator ρ, defined by

$$\rho = \overline{|\psi\rangle\langle\psi|} \tag{9}$$

where $|\psi\rangle$ is the quantum state of an individual system, written as a ket in Hilbert space, and the overbar denotes an ensemble average. In the current case of a spin-1/2 pair, the Hilbert space has dimension $N_{\mathbb{H}} = 4$, so the corresponding Liouville space of spin operators has dimension $N_{\mathbb{L}} = N_{\mathbb{H}}^2 = 16$. The density operator may be written as a Liouville space ket, denoted $\big|\rho(t)\big)$.

The evolution of the spin ensemble may be described by the Liouville-von Neumann equation,

$$\frac{d}{dt}\big|\rho(t)\big) = \hat{\mathcal{L}}\big|\rho(t)\big), \tag{10}$$

where $\hat{\mathcal{L}}$ is the Liouvillian, given by,

$$\hat{\mathcal{L}} = \hat{\mathcal{L}}_{\text{coh}} + \hat{\Gamma}, \tag{11}$$

where $\hat{\mathcal{L}}_{\text{coh}}$ is the *coherent Liouvillian*, given by,

$$\hat{\mathcal{L}}_{\text{coh}} = -i\hat{H}_{\text{coh}}. \tag{12}$$

Here $\hat{H}_{\text{coh}}$ is the commutation superoperator of the coherent Hamiltonian, defined by,

$$\hat{H}_{\text{coh}}\big|A\big) = \big[H_{\text{coh}}, A\big], \tag{13}$$

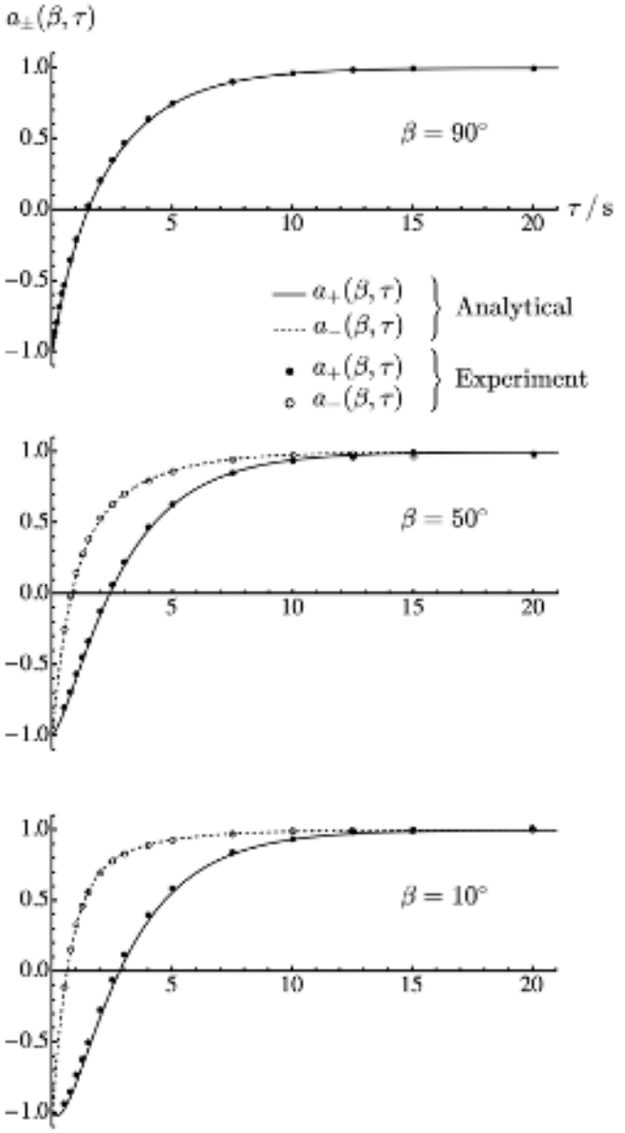

FIG. 6. Experimental (points) and analytical peak trajectories (curves) using eq. (48) and parameters in table II for the variable flip-angle inversion-recovery experiments at 9.4 T, obtained by the pulse sequence in figure 2. Analytical curves were computed using routines in *SpinDynamica* [35].

with A an arbitrary operator.

The superoperator $\hat{H}_{\text{coh}}$ generates the coherent dynamics, while the *relaxation superoperator* $\hat{\Gamma}$ generates the dissipative dynamics. These two terms do not commute in general, which leads to a rich interplay between the coherent and dissipative dynamics.

In general, the Liouvillian superoperator has a set of $N_{\mathbb{L}}$ eigenoperators and eigenvalues:

$$\hat{\mathcal{L}}|Q_q) = \Lambda_q|Q_q) \qquad q \in \{0, 1, \cdots, N_{\mathbb{L}} - 1\}, \tag{14}$$

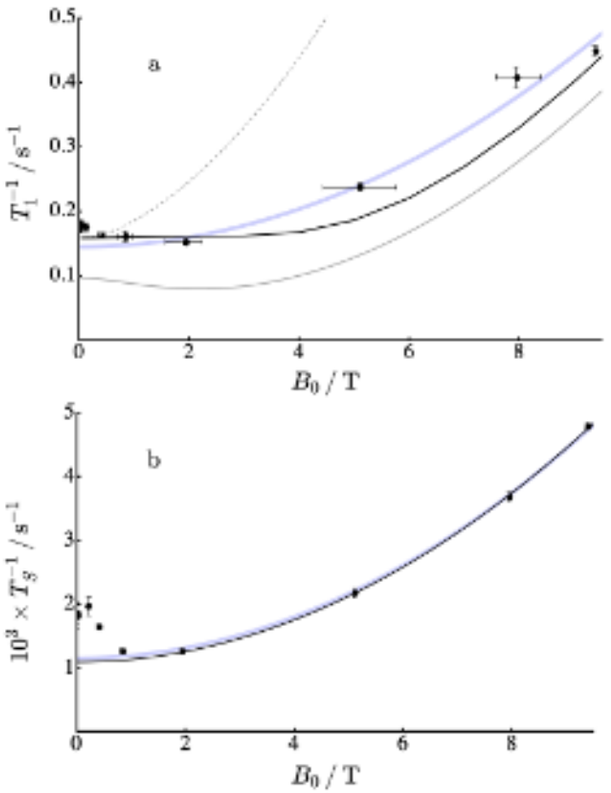

FIG. 7. Relaxation rate constants T_1^{-1} and T_S^{-1} as a function of magnetic field. (a) Filled circles with confidence limits: Experimental values of T_1^{-1} as a function of field B_0. Light blue curve: Polynomial $T_1^{-1}(B_0) = aB_0^2 + c$ with parameters $a = 3.67 \times 10^{-3}\,\mathrm{s^{-1}\,T^{-1}}$ and $c = 0.146\,\mathrm{s^{-1}}$, obtained by fitting the experimental data above 1.5 T. Grey dashed line: Theoretical field-dependence of the rate constant $\lambda^{(1)}$ (table V). Grey solid line: Theoretical field-dependence of the rate constant $\lambda^{(2)}$ (table V). Black solid line: Theoretical field dependence of T_1^{-1}, obtained by fitting the analytical inversion-recovery trajectories of eq. (49) to a single-exponential form, for the flip angle $\beta = \pi/2$. (b) Filled circles with confidence limits: Experimental values of T_S^{-1} as a function of field B_0. Light blue curve: Polynomial fit $T_S^{-1}(B_0) = aB_0^2 + c$ with the parameters $a = 40.6 \times 10^{-6}\,\mathrm{s^{-1}\,T^{-2}}$, $c = 1.16 \times 10^{-3}\,\mathrm{s^{-1}}$, obtained by fitting the experimental data above 0.8 T. Black solid line: Theoretical field dependence of T_S^{-1}. All theoretical curves use the parameters given in table II.

with,

$$\Lambda_q = -\lambda_q + i\omega_q, \tag{15}$$

where λ_q and ω_q are both real.

Consider the commutation superoperator for the spin angular momentum operator along the main magnetic field:

$$\hat{I}_z|A) = |[I_z, A]) \tag{16}$$

where A is an operator. In the high-field approximation [40], $\hat{I}_z$ commutes with the Liouvillian superoperator $\hat{\mathcal{L}}$:

$$[\hat{I}_z, \hat{\mathcal{L}}] = 0 \tag{17}$$

A consequence of eq. (17) is that the Liouvillian eigenoperators $|Q_q)$ may be classified by their *coherence order* p_q, defined as their eigenvalue under the commutation superoperator $\hat{I}_z$:

$$\hat{I}_z|Q_q) = p_q|Q_q) \tag{18}$$

For an ensemble of spin-1/2 pairs, the coherence orders take values $p_q \in \{-2, -1, 0, +1, +2\}$.

The previous paper [1] was mainly concerned with the dynamics of eigenoperators with $p_q = -1$, which are single-quantum coherences oscillating at frequency ω_q and which are capable of generating a quadrature-detected NMR signal. The current paper, on the other hand, is mainly concerned with zero-quantum (ZQ) eigenoperators with $p_q = 0$. Those eigenoperators with eigenvalues for which $\omega_q = 0$ represent configurations of spin-state populations, whilst those with eigenvalues for which $\omega_q \neq 0$ represent ZQ coherences which oscillate at ω_q. In both cases, the configurations relax back towards thermal equilibrium under the dissipative effects of $\hat{\Gamma}$ with rate constant $\lambda_q > 0$. As described below, it is important that the form of $\hat{\Gamma}$ correctly takes into account the finite temperature of the molecular environment.

Consider the spin dynamics in the following basis of normalized zero-quantum spherical tensor operator components:

$$\mathbb{B}_0 = \left\{ \mathbb{T}^0_{00}, \mathbb{T}^g_{00}, \mathbb{T}^g_{10}, \mathbb{T}^u_{10}, \mathbb{T}^{u\dagger}_{10}, \mathbb{T}^g_{20} \right\}, \tag{19}$$

where the basis operators are:

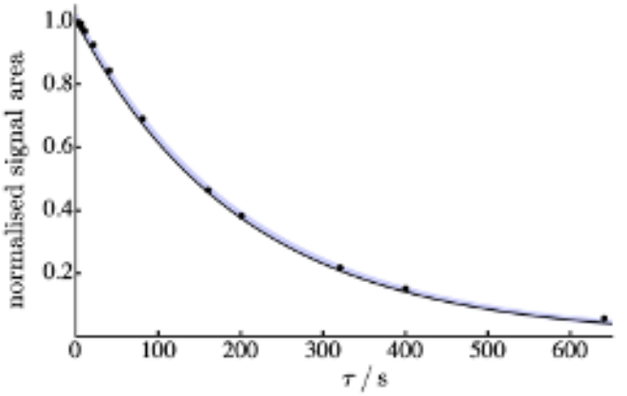

FIG. 8. Singlet order decay curve obtained by the pulse sequence in figure 3 at 9.4 T. The light blue line shows the mono-exponential decay function (eq. (3)) with time constant $T_S = 209\,\mathrm{s}$. The black curve shows the theoretical decay function from eq. (55), for the best-fit parameters given in Table II.

TABLE II. Spin system parameters for **I** in solution.

Parameter	Value	Note
J_{jk}	214.15 Hz	Experimental [a]
$\Delta\delta_{\rm iso}$	0.16 ppm	Experimental [b]
$b_{jk}/(2\pi)$	−4152.84 Hz	Estimated [c]
$\delta_j^{\rm CSA}$	−145.7 ppm	Calculated for the equilibrium structure [d]
η_j	0.020	Calculated for the equilibrium structure [d]
$\delta_k^{\rm CSA}$	−145.4 ppm	Calculated for the equilibrium structure [d]
η_k	0.023	Calculated for the equilibrium structure [d]
$\tau_\perp$	155 ps	Best fit [e]
$\omega_{\rm rand}^2\tau_{\rm rand}$	0.549×10^{-3} Hz	Best fit [e]
$\Delta\delta_{\rm CSA}$	13.3 ppm	Best fit [f]
κ_{jk}	0	Assumed for simplicity

[a] Obtained from a 90° pulse-acquire spectrum on a 700 MHz spectrometer. [b] Estimated from the ^{13}C spectrum of natural abundance material; [c] Estimated from the internuclear distance, $r_{jk} = 122$ pm. [d] Geometry optimization and magnetic shielding tensors were calculated at the B3LYP/aug-cc-PVTZ level of theory using the Gaussian 09 software [1, 39]. [e] Best fit to the 9.4 T, $\beta = 10°, 50°, 90°$ flip-angle experiments using eq. (48). [f] Best fit to the singlet relaxation field-dependent data using eq. (56).

$$
\begin{aligned}
\mathbb{T}_{00}^{0} &= \tfrac{1}{2}\mathbb{1} \\
&= \tfrac{1}{2}\left(|S_0\rangle\langle S_0| + |T_{+1}\rangle\langle T_{+1}| + |T_0\rangle\langle T_0| + |T_{-1}\rangle\langle T_{-1}|\right) \\
\mathbb{T}_{00}^{g} &= -\frac{2}{\sqrt{3}}\mathbf{I}_j\cdot\mathbf{I}_k \\
&= -\frac{1}{2\sqrt{3}}\left(3|S_0\rangle\langle S_0| - |T_{+1}\rangle\langle T_{+1}|\right. \\
&\qquad \left. -|T_0\rangle\langle T_0| - |T_{-1}\rangle\langle T_{-1}|\right), \\
\mathbb{T}_{10}^{g} &= \frac{1}{\sqrt{2}}(I_{jz} + I_{kz}) \\
&= \frac{1}{\sqrt{2}}\left(|T_{+1}\rangle\langle T_{+1}| - |T_{-1}\rangle\langle T_{-1}|\right), \\
\\
\mathbb{T}_{10}^{u} &= \frac{1}{2}(I_{jz} - I_{kz}) + \frac{1}{2}\left(I_j^- I_k^+ - I_j^+ I_k^-\right) \\
&= |T_0\rangle\langle S_0|, \\
\\
\mathbb{T}_{10}^{u\dagger} &= \frac{1}{2}(I_{jz} - I_{kz}) - \frac{1}{2}\left(I_j^- I_k^+ - I_j^+ I_k^-\right) \\
&= |S_0\rangle\langle T_0|, \\
\mathbb{T}_{20}^{g} &= \sqrt{\frac{2}{3}}\left(3I_{jz}I_{kz} - \mathbf{I}_j\cdot\mathbf{I}_k\right) \\
&= \frac{1}{\sqrt{6}}\left(|T_{+1}\rangle\langle T_{+1}| - 2|T_0\rangle\langle T_0| + |T_{-1}\rangle\langle T_{-1}|\right),
\end{aligned}
\tag{20}
$$

The spherical tensor operator components satisfy the rotational property [22],

$$
\hat{R}_\phi(\Omega)\mathbb{T}_{lm} = \sum_{m'=-l}^{+l} D^{(l)}_{m'm}(\Omega)\mathbb{T}_{lm'}. \tag{21}
$$

The superscripts u and g in eq. (20) indicate a two-spin operator which is odd or even, respectively, under exchange of the two spins. The odd-parity rank-1 spherical tensor operator components $\mathbb{T}_{10}^u$ and $\mathbb{T}_{10}^{u\dagger}$ were introduced previously in the context of symmetry-based singlet-triplet excitation [41]. These two operators represent the zero-quantum coherences.

The $\mathbb{T}_{00}^g$ operator has an expectation value proportional to the population imbalance between the singlet and triplet manifolds, and referred to as *singlet order*. The $\mathbb{T}_{10}^g$ operator has an expectation value proportional to longitudinal magnetisation, and referred to as *longitudinal order*. The $\mathbb{T}_{20}^g$ operator has an expectation value proportional to the deviation in population of the central triplet state $|T_0\rangle$ from the mean population of the outer triplet states $|T_{\pm1}\rangle$. The operator $\mathbb{T}_{00}^0$ is proportional to the unity operator, and represents the sum of populations over all states, which is conserved under all processes.

C. Coherent Liouvillian

The ZQ block of the matrix representation of $\hat{\mathcal{L}}_{\rm coh}$, as defined in eq. (12), is given by

$$\hat{\mathcal{L}}_{\rm coh} = -i \begin{array}{c} \begin{matrix} \mathbb{T}^0_{00} & \mathbb{T}^g_{00} & \mathbb{T}^g_{10} & \mathbb{T}^u_{10} & \mathbb{T}^{u\dagger}_{10} & \mathbb{T}^g_{20} \end{matrix} \\ \begin{pmatrix} 0 & 0 & 0 & 0 & 0 & 0 \\ 0 & 0 & 0 & \frac{1}{\sqrt{3}}\omega_\Delta & -\frac{1}{\sqrt{3}}\omega_\Delta & 0 \\ 0 & 0 & 0 & 0 & 0 & 0 \\ 0 & \frac{1}{\sqrt{3}}\omega_\Delta & 0 & \omega_J & 0 & \frac{1}{\sqrt{6}}\omega_\Delta \\ 0 & -\frac{1}{\sqrt{3}}\omega_\Delta & 0 & 0 & -\omega_J & -\frac{1}{\sqrt{6}}\omega_\Delta \\ 0 & 0 & 0 & \frac{1}{\sqrt{6}}\omega_\Delta & -\frac{1}{\sqrt{6}}\omega_\Delta & 0 \end{pmatrix} \end{array} \tag{22}$$

In the near-equivalence limit, $|\omega_J| \gg |\omega_\Delta|$, the basis operators of $\mathbb{B}_0$, given in eq. (20), define an approximate eigenbasis of the coherent zero-quantum Liouvillian.

D. Relaxation Superoperator

1. Lindbladian thermalization

In reference [1] we treated the dissipative dynamics of the spin system by using a relaxation superoperator constructed with the Redfield-Abragam formalism [20, 21, 42, 43]. Although this method is sufficient for treating the decay of coherences, it displays irrecoverable flaws when treating the dynamics of spin-state populations for the case of a spin system interacting with a finite-temperature environment. The usual remedy is to introduce a thermal equilibrium term $\rho_{\rm eq}$ into the Liouville von Neumann equation (10), leading to the so-called inhomogeneous master equation (IME) [20–22, 42]. However, it has been shown that the IME is not consistent with the theory of open quantum systems [44–47] and in some cases leads to unphysical results [23]. In the current paper we avoid such uncertainties by constructing the relaxation superoperator through a Lindbladian formalism [23, 48]. This allows a rigorous treatment of a spin system in contact with a finite-temperature environment, without the introduction of *ad hoc* terms.

It should be noted, however, that since the current experiments only involve spin systems with very small amounts of spin order, the standard IME approach and the Lindbladian formalism give indistinguishable results. The Lindbladian approach is used here for theoretical consistency and in anticipation of experiments on hyperpolarized systems, where the validity of the standard IME is insecure [23].

The Lindbladian form of the relaxation superoperator in an isotropic medium of finite temperature is given by,

$$\hat{\Gamma}^\theta \simeq \hat{\Gamma}^\theta_{\rm intra} + \hat{\Gamma}^\theta_{\rm rand} \tag{23}$$

where $\hat{\Gamma}^\theta_{\rm intra}$ is the contribution to the relaxation superoperator from intramolecular relaxation mechanisms, and $\hat{\Gamma}^\theta_{\rm rand}$ is the relaxation superoperator for the intermolecular contributions, approximated by a random-field mechanism. The symbol θ signifies "thermalization" [23] and indicates that the relaxation superoperator takes into account the finite temperature of the environment. The following equations use the symbol β_θ for the inverse temperature parameter,

$$\beta_\theta = \hbar / k_B T, \tag{24}$$

where k_B is the Boltzmann constant.

2. Intramolecular relaxation

The intramolecular relaxation superoperator is given by,

$$\hat{\Gamma}^\theta_{\rm intra} = \sum_{\Lambda\,\Lambda'} \hat{\Gamma}^\theta_{\Lambda\Lambda'}, \tag{25}$$

where each term has the form,

$$\hat{\Gamma}^\theta_{\Lambda\Lambda'} = \delta_{\ell\,\ell'} c^\Lambda c^{\Lambda'} \sum_{\ell,m} J^{\theta\Lambda\Lambda'}_{\ell\ell' m}(\omega_0)\; \hat{\mathcal{D}}\Big[\big[X^\Lambda_{\ell m}\big]^L, \big[X^{\Lambda'\dagger}_{\ell' m}\big]^L\Big]. \tag{26}$$

Each term $\hat{\Gamma}^\theta_{\Lambda\Lambda'}$ involves two spin interactions Λ and Λ', which have spatial ranks ℓ and ℓ' respectively. The Kronecker delta $\delta_{\ell\,\ell'}$ ensures that only terms of the same spatial rank ℓ contribute to the relaxation superoperator. Terms $\hat{\Gamma}^\theta_{\Lambda\Lambda'}$ with $\ell = \ell'$ but $\Lambda \neq \Lambda'$ represent cross-correlation contributions to the relaxation superoperator.

The terms $J^{\theta\Lambda\Lambda'}_{\ell\ell' m}(\omega_0)$ are the thermalised spectral density functions given below, $\big[X^\Lambda_{\ell m}\big]^L$ are the $m^{\rm th}$-components of $\ell^{\rm th}$-rank irreducible spherical spin (or spin-field) tensors for interaction Λ in the laboratory (L-) frame (see our previous article, ref. [1]), and $\hat{\mathcal{D}}$ is the Lindbladian dissipator [23, 27], defined as follows:

$$\hat{\mathcal{D}}\big[A, B^\dagger\big]\, Q = AQB^\dagger - \frac{1}{2}\left(AB^\dagger Q + QAB^\dagger\right), \tag{27}$$

where A, B and Q are arbitrary operators.

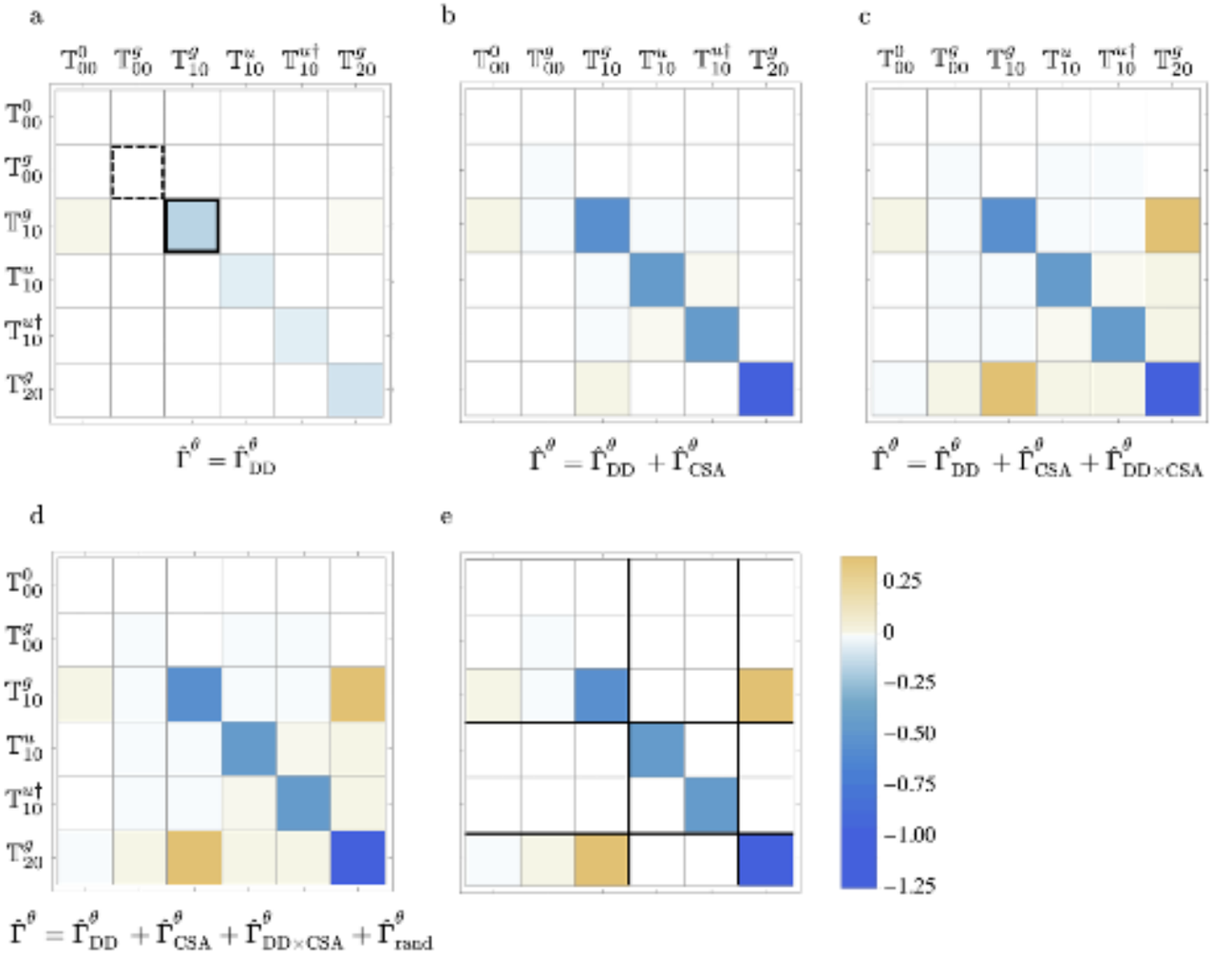

FIG. 9. Numerical matrix representations of the zero-quantum blocks of the relaxation superoperators in the $\mathbb{B}_0$ basis given in eq. (19) and (20), for the parameters in table II. (a) Thermalized relaxation superoperator $\hat{\Gamma}^{\theta}_{\mathrm{DD}}$ for the intra-pair DD mechanism. Diagonal elements corresponding to singlet order $\mathbb{T}^{g}_{00}$ and longitudinal order, $\mathbb{T}^{g}_{10}$ are indicated by dashed and solid borders respectively. (b) With inclusion of the CSA mechanism. Off-diagonal elements for these two mechanisms which are not removed under secularization are at least five orders-of-magnitude smaller than the diagonal elements and considered negligible. (c) With inclusion of the DD-CSA cross-correlation, showing the off-diagonal elements connecting the $\mathbb{T}^{g}_{10}$ and $\mathbb{T}^{g}_{20}$ operators. (d) With fluctuating random fields included. (e) Matrix representation of the relaxation superoperator after zero-quantum secularization (section IV D 5).

Assuming that $\mathbf{I}$ may be approximated as a symmetric top, the spectral density terms $J^{\theta\Lambda\Lambda'}_{\ell\ell' m}(\omega_0)$ for the intramolecular interactions are given by,

$$J^{\theta\Lambda\Lambda'}_{\ell\ell' m}(\omega_0) = (2\ell+1)^{-1} \sum_{n} \left[A^{\Lambda *}_{\ell n}\right]^{D} \left[A^{\Lambda'}_{\ell' n}\right]^{D} \times \frac{2\tau^{(\ell)}_{\perp}}{1 + m^2\omega_0^2 \tau^{(l)2}_{\perp}} \exp\left\{-\frac{1}{2}\beta_\theta m \omega_0\right\}, \tag{28}$$

In eq. 28, $\tau_\perp$ is the rotational correlation time associated with diffusion about axes perpendicular to the molecular long axis, and $\left[A^{\Lambda *}_{\ell n}\right]^{D}$ are spatial functions in the principal axis frame D of the rotational diffusion tensor. These may be expanded in terms of functions in the common principal axis frame P of the anisotropic spin interactions,

$$\left[A^{\Lambda}_{\ell n}\right]^{D} = \sum_{n'} \left[A^{\Lambda}_{\ell n'}\right]^{P} D^{(\ell)}_{n' n}(\Omega_{PD}) \,. \tag{29}$$

Here $D^{(\ell)}_{n' n}(\Omega_{PD})$ are Wigner functions with angles Ω_{PD} as arguments which parameterise the orientation of the two frames with respect to one another. It may be shown that for rigid linear molecules the only non-vanishing terms in eq. (28) are for $n = 0$. Details of the derivation leading to eq. (28) are given in the supplementary

material of our previous paper [1].

3. Random-field relaxation

In this paper, relaxation by spin-rotation [49–51] and fluctuating intermolecular couplings [43, 52] is approximated by a mechanism involving randomly fluctuating fields which are partially correlated at the two spin sites. The appropriate relaxation superoperator is as follows [23]:

$$\hat{\Gamma}^{\theta}_{\text{rand}} = \sum_{j,k=1}^{2} \kappa_{jk} \omega^{(j)}_{\text{rms}} \omega^{(k)}_{\text{rms}} \times \sum_{m=-1}^{+1} J^{\theta}_{m,\text{rand}}\left(\omega_0\right) \hat{\mathcal{D}}\Big[\big[X^{\text{rand}}_{1m}\big]^{L}, \big[X^{\text{rand}\dagger}_{1m}\big]^{L}\Big], \tag{30}$$

where $\omega^{(j)}_{\text{rms}}$ and $\omega^{(k)}_{\text{rms}}$ are the root-mean-square amplitudes of the local field fluctuations associated with spins j and k respectively, and $J^{\theta}_{m,\text{rand}}\left(\omega_0\right)$ is the thermalised spectral density function given by,

$$J^{\theta}_{m,\text{rand}}\left(\omega_0\right) = \frac{2\tau_{\text{rand}}}{1 + m^2\omega_0^2\tau_{\text{rand}}^2} \exp\left\{-\frac{1}{2}\beta_\theta m\omega_0\right\}, \tag{31}$$

where τ_{rand} is the random field correlation time.

The spin tensor components in eq. (30) are given by,

$$\begin{aligned} \big[X^{\Lambda}_{10}\big]^{L} &= I_{jz}, \\ \big[X^{\Lambda}_{1\pm1}\big]^{L} &= \mp\frac{1}{\sqrt{2}} I^{\pm}_{j}. \end{aligned} \tag{32}$$

The symbol $-1 \leq \kappa_{jk} \leq +1$ is a coefficient describing the degree of correlation of fluctuations experienced by both spins. $\kappa_{jk} = 1$ represents perfectly correlated random fields while $\kappa_{jk} = -1$ represents perfect anti-correlation. By definition, the autocorrelations are equal to one, $\kappa_{jj} = \kappa_{kk} = 1$.

4. Relaxation matrices

Figure 9(a,b,c) shows graphical representations of the ZQ blocks of the relaxation superoperators, evaluated numerically for the interaction parameters specified in table II and the supplementary material of our previous article [1].

Figure 9(a) shows the matrix representation of the Lindblad-thermalized DD relaxation superoperator $\hat{\Gamma}^{\theta}_{\text{DD}}$, in the zero-quantum operator basis $\mathbb{B}_0$. The element with the dashed outline corresponds to the relaxation rate constant of singlet-order, $\mathbb{T}^{g}_{00}$, which vanishes under the DD mechanism. The element with a solid outline corresponds to the relaxation rate constant of longitudinal order, $\mathbb{T}^{g}_{10}$. Note the small off-diagonal elements $\big(\mathbb{T}^{g}_{10}\big|\hat{\Gamma}^{\theta}_{\text{DD}}\big|\mathbb{T}^{0}_{00}\big)$ and $\big(\mathbb{T}^{g}_{10}\big|\hat{\Gamma}^{\theta}_{\text{DD}}\big|\mathbb{T}^{g}_{20}\big)$, indicated by the faint colours. These off-diagonal elements are asymmetric about the diagonal. They are very small for the simulated parameters ($\sim 10^{-6}\,\text{s}^{-1}$) and arise from the thermalisation of the relaxation superoperator using Lindbladian dissipators (eq. (27)), required for the rigorous representation of the contact of the spin system with a finite-temperature environment [23, 27, 48, 53]. It is not yet known whether these small matrix elements are associated with NMR phenomena.

Figure 9(b) shows the zero-quantum block of the relaxation superoperator after inclusion of the CSA mechanism. The off-diagonal elements are still small compared to the diagonal ones, indicating that $\mathbb{B}_0$ is close to an eigenoperator basis of the ZQ block.

Figure 9(c) shows the inclusion of DD-CSA cross-correlation, as well as the DD and CSA auto-correlation terms. Cross-correlated relaxation introduces significant off-diagonal elements between the $\mathbb{T}^{g}_{10}$ and $\mathbb{T}^{g}_{20}$ operators.

5. Zero-quantum secular approximation

The full Liouvillian is a superposition of the coherent part, whose zero-quantum block is given in eq. (22), and the dissipative part, given by the relaxation superoperator.

As shown in eq. (22), the diagonal matrix elements for the operators $\mathbb{T}^{u}_{10}$ and $\mathbb{T}^{u\dagger}_{10}$ are given by

$$\begin{aligned} \big(\mathbb{T}^{u}_{10}\big|\hat{\mathcal{L}}_{\text{coh}}\big|\mathbb{T}^{u}_{10}\big) &= -i\omega_J \\ \big(\mathbb{T}^{u\dagger}_{10}\big|\hat{\mathcal{L}}_{\text{coh}}\big|\mathbb{T}^{u\dagger}_{10}\big) &= +i\omega_J \end{aligned} \tag{33}$$

while the corresponding diagonal matrix elements for all the other zero-quantum operators are zero. In the near-equivalence limit, $|\omega_J|$ greatly exceeds the coherent off-diagonal term $|\omega_\Delta|$ and also all off-diagonal components of the relaxation superoperator. It follows that, to a good approximation, all off-diagonal Liouvillian terms connecting the operators $\mathbb{T}^{u}_{10}$ and $\mathbb{T}^{u\dagger}_{10}$ with other zero-quantum operators may be ignored:

$$\begin{aligned} \big(\mathbb{T}^{u}_{10}\big|\hat{\mathcal{L}}\big|Q_q\big) &\rightarrow 0 \;;\; \forall\; Q_q \neq \mathbb{T}^{u}_{10} \\ \big(\mathbb{T}^{u\dagger}_{10}\big|\hat{\mathcal{L}}\big|Q_q\big) &\rightarrow 0 \;;\; \forall\; Q_q \neq \mathbb{T}^{u\dagger}_{10} \\ \big(Q_q\big|\hat{\mathcal{L}}\big|\mathbb{T}^{u}_{10}\big) &\rightarrow 0 \;;\; \forall\; Q_q \neq \mathbb{T}^{u}_{10} \\ \big(Q_q\big|\hat{\mathcal{L}}\big|\mathbb{T}^{u\dagger}_{10}\big) &\rightarrow 0 \;;\; \forall\; Q_q \neq \mathbb{T}^{u\dagger}_{10} \end{aligned} \tag{34}$$

The effect of this approximation is to decouple the ZQ coherences from the populations. In principle, the off-diagonal elements of the coherent Liouvillian, given in eq. (22), give rise to singlet-triplet leakage terms which appear to second-order in the chemical shift difference. These second-order leakage terms are ignored in the following discussion.

This approximation leads to a considerable simplification of the zero-quantum spin dynamics and is called

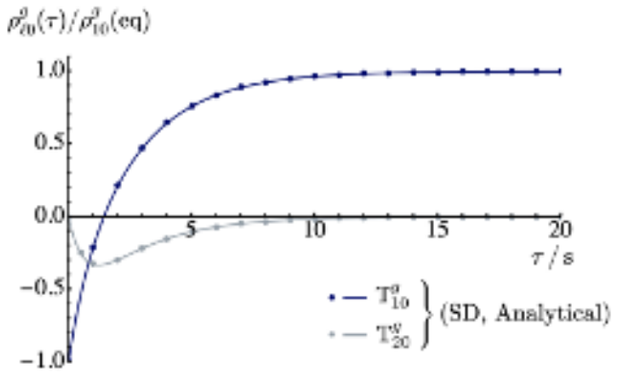

FIG. 10. Polarization moment trajectories after the π-pulse in an inversion-recovery experiment, calculated for the parameters in table II. Points: Numerical *SpinDynamica* simulations, using the full 16-dimensional Liouvillian. Solid lines: Analytical polarization moment trajectories using eq.(44). Both polarization moments are given relative to the equilibrium rank-1 polarization moment, defined in equation 45. The numerical and analytical trajectories are indistinguishable. The trajectories show that rank-1 polarization is converted into negative rank-2 polarization by cross-correlated DD-CSA relaxation.

here the *zero-quantum secular approximation.* The implementation of the zero-quantum secular approximation at the level of the relaxation superoperator is illustrated in figure 9(e).

E. Relaxation of Longitudinal magnetization

We now consider the peak trajectories in an inversion-recovery experiment, as shown in figures 4 and 6. For simplicity, the following analytical treatment of the relaxation of longitudinal spin order makes the following approximations:

- The high-temperature approximation is made:

$$|\omega_0\beta_\theta| << 1 \tag{35}$$

- The biaxiality parameters of the two CSA tensors are ignored: $\eta_j = \eta_k = 0$.

All parameters used for the analytical curves and simulations are given in table II. For simplicity, we assume uncorrelated fields, $\kappa_{jk} = 0$, and $\tau_\perp$ and $\omega^2_{\mathrm{rand}}\tau_{\mathrm{rand}}$ become the only two fitted parameters.

1. Polarization moment trajectories

Invoking the *high-field* and *high-temperature* approximations, the thermal equilibrium density operator may be expressed as,

$$\begin{aligned}\big|\rho_{\mathrm{eq}}\big) &\simeq N_{\mathbb{H}}^{-1}\,\big|\mathbb{1} - \beta_\theta\omega_0 I_z\big) \\ &= \frac{1}{2}\big(\mathbb{T}^0_{00} - \frac{1}{\sqrt{2}}\omega_0\beta_\theta\mathbb{T}^g_{10}\big),\end{aligned} \tag{36}$$

using the spherical tensor operators in eq. (19). Upon application of a π-pulse, by virtue of eq. (21) we have,

$$\begin{aligned}\big|\rho_{\mathrm{inv}}\big) &= \hat{R}_\phi(\pi)\big|\rho_{\mathrm{eq}}\big) \\ &= \frac{1}{2}\big(\mathbb{T}^0_{00} + \frac{1}{\sqrt{2}}\omega_0\beta_\theta\mathbb{T}^g_{10}\big).\end{aligned} \tag{37}$$

The density operator at a time τ after the π-pulse may be written as follows:

$$\big|\rho(\tau)\big) = e^{\hat{\mathcal{L}}\tau}\big|\rho_{\mathrm{inv}}\big) = \sum_\ell \rho_{\ell 0}(\tau)\big|\mathbb{T}_{\ell 0}\big), \tag{38}$$

where $\rho_{\ell 0}(\tau)$ are the *polarization moments* [54, 55] defined as follows:

$$\rho_{\ell 0}(\tau) = \big(\mathbb{T}_{\ell 0}|\rho(\tau)\big) = \big(\mathbb{T}_{\ell 0}|e^{\hat{\mathcal{L}}\tau}\big|\rho_{\mathrm{inv}}\big). \tag{39}$$

The trajectories of the polarization moments indicate the mixing of different spin ranks during the recovery interval τ.

Within the zero-quantum secular approximation, the relaxation dynamics of longitudinal magnetization may be analyzed in terms of the following 3×3 block of the Liouvillian matrix, spanned by the operators $\mathbb{T}^0_{00}$, $\mathbb{T}^g_{10}$ and $\mathbb{T}^g_{20}$:

$$\mathbf{L} = \begin{pmatrix} 0 & 0 & 0 \\ \theta_{10} & -\lambda_{10} & \Delta \\ \theta_{20} & \Delta' & -\lambda_{20} \end{pmatrix}, \tag{40}$$

The diagonal elements are given by $\lambda_{\ell 0} = \lambda^{\mathrm{DD}}_{\ell 0} + \lambda^{\mathrm{CSA}}_{\ell 0} + \lambda^{\mathrm{rand}}_{\ell 0}$. Analytical expressions for the elements are given in tables III and IV.

The zero-quantum Liouvillian matrix $\mathbf{L}$ may be diagonalized through,

$$\mathbf{L} = \mathbf{S}\mathbf{\Lambda}\mathbf{S}^{-1} \tag{41}$$

where $\mathbf{\Lambda}$ is a diagonal matrix with the eigenvalues of $\mathbf{L}$ on the diagonal:

$$\mathbf{\Lambda} = \begin{pmatrix} 0 & 0 & 0 \\ 0 & -\lambda^{(1)} & 0 \\ 0 & 0 & -\lambda^{(2)} \end{pmatrix}, \tag{42}$$

and $\mathbf{S}$ is a matrix whose columns are the eigenvectors of $\mathbf{L}$:

$$\mathbf{S} = \begin{pmatrix} S_{11} & 0 & 0 \\ S_{21} & S_{22} & S_{23} \\ 1 & 1 & 1 \end{pmatrix}. \tag{43}$$

The elements of $\mathbf{\Lambda}$ and $\mathbf{S}$ are given in table V. The eigenvector of $\mathbf{L}$ corresponding to the zero eigenvalue represents the thermal equilibrium state. The terms $\lambda^{(1)}$ and

TABLE III. The negative of the diagonal elements of the 3×3 zero-quantum block of the Liouvillian, as given in eq. (40). All expressions utilise the high-temperature approximation.

$$\lambda_{10}^{\mathrm{DD}} \simeq -(\mathbb{T}_{10}^{g}|\hat{\Gamma}_{\mathrm{DD}}^{\theta}|\mathbb{T}_{10}^{g}) = \frac{3}{10} b_{jk}^2 \left\{ \frac{\tau_\perp}{1+\tau_\perp^2\omega_0^2} + \frac{4\tau_\perp}{1+4\tau_\perp^2\omega_0^2} \right\}$$

$$\lambda_{20}^{\mathrm{DD}} \simeq -(\mathbb{T}_{20}^{g}|\hat{\Gamma}_{\mathrm{DD}}^{\theta}|\mathbb{T}_{20}^{g}) = \frac{9}{10} b_{jk}^2 \frac{\tau_\perp}{1+\tau_\perp^2\omega_0}$$

$$\lambda_{10}^{\mathrm{CSA}} \simeq -(\mathbb{T}_{10}^{g}|\hat{\Gamma}_{\mathrm{CSA}}^{\theta}|\mathbb{T}_{10}^{g}) = \frac{3}{20}\omega_0^2 \left(\left[\delta_j^{\mathrm{CSA}}\right]^2 + \left[\delta_k^{\mathrm{CSA}}\right]^2 \right) \frac{\tau_\perp}{1+\tau_\perp^2\omega_0^2}$$

$$\lambda_{20}^{\mathrm{CSA}} \simeq -(\mathbb{T}_{20}^{g}|\hat{\Gamma}_{\mathrm{CSA}}^{\theta}|\mathbb{T}_{20}^{g}) = \frac{1}{60}\omega_0^2 \left\{ 4\,\tau_\perp \left(\delta_j^{\mathrm{CSA}} - \delta_k^{\mathrm{CSA}}\right)^2 + \left(5\left[\delta_j^{\mathrm{CSA}}\right]^2 + 5\left[\delta_k^{\mathrm{CSA}}\right]^2 + 8\delta_j^{\mathrm{CSA}}\delta_k^{\mathrm{CSA}} \right) \frac{3\tau_\perp}{1+\tau_\perp^2\omega_0^2} \right\}$$

$$\lambda_{10}^{\mathrm{rand}} \simeq -(\mathbb{T}_{10}^{g}|\hat{\Gamma}_{\mathrm{rand}}^{\theta}|\mathbb{T}_{10}^{g}) = 2\,\omega_{\mathrm{rand}}^2\tau_{\mathrm{rand}}$$

$$\lambda_{20}^{\mathrm{rand}} \simeq -(\mathbb{T}_{20}^{g}|\hat{\Gamma}_{\mathrm{rand}}^{\theta}|\mathbb{T}_{20}^{g}) = 2\,(2+\kappa_{jk})\,\omega_{\mathrm{rand}}^2\tau_{\mathrm{rand}}$$

TABLE IV. The off-diagonal elements of the 3×3 zero-quantum block of the Liouvillian in the high-temperature approximation, as given in eq. (40), with $\theta_{10} = \theta_{10}^{\mathrm{DD}} + \theta_{10}^{\mathrm{CSA}} + \theta_{10}^{\mathrm{rand}}$. The thermal terms θ_{10} and θ_{20} are small compared to the others, but are necessary for a correct treatment of thermal equilibration. All expressions are given in the high-temperature approximation.

$$\theta_{10}^{\mathrm{DD}} + \theta_{10}^{\mathrm{CSA}} = (\mathbb{T}_{10}^{g}|\hat{\Gamma}_{\mathrm{DD}}^{\theta} + \hat{\Gamma}_{\mathrm{CSA}}^{\theta}|\mathbb{T}_{00}^{0}) = -\frac{3}{10\sqrt{2}} b_{jk}^2\omega_0\beta_\theta \left\{ \frac{\tau_\perp}{1+\tau_\perp^2\omega_0^2} + \frac{4\tau_\perp}{1+4\tau_\perp^2\omega_0^2} \right\} - \frac{3}{20\sqrt{2}}\omega_0^3\beta_\theta \left(\left[\delta_j^{\mathrm{CSA}}\right]^2 + \left[\delta_k^{\mathrm{CSA}}\right]^2 \right) \frac{\tau_\perp}{1+\tau_\perp^2\omega_0^2}$$

$$\theta_{10}^{\mathrm{rand}} = (\mathbb{T}_{10}^{g}|\hat{\Gamma}_{\mathrm{rand}}^{\theta}|\mathbb{T}_{00}^{0}) = -\sqrt{2}\,\omega_0\beta_\theta\omega_{\mathrm{rand}}^2\tau_{\mathrm{rand}}$$

$$\theta_{20} = (\mathbb{T}_{20}^{g}|\hat{\Gamma}_{\mathrm{DD\times CSA}}^{\theta}|\mathbb{T}_{00}^{0}) = -\frac{3}{10}\sqrt{\frac{3}{2}} b_{jk}\omega_0^2\beta_\theta \left(\delta_j^{\mathrm{CSA}} + \delta_k^{\mathrm{CSA}}\right) \frac{\tau_\perp}{1+\tau_\perp^2\omega_0^2}$$

$$\Delta = (\mathbb{T}_{10}^{g}|\hat{\Gamma}_{\mathrm{DD\times CSA}}^{\theta} + \hat{\Gamma}_{\mathrm{rand}}^{\theta}|\mathbb{T}_{20}^{g}) = -\frac{3\sqrt{3}}{10}\omega_0 b_{jk} \left(\delta_j^{\mathrm{CSA}} + \delta_k^{\mathrm{CSA}}\right) \frac{\tau_\perp}{1+\tau_\perp^2\omega_0^2} + \frac{1}{\sqrt{3}}\omega_0\beta_\theta\,\kappa_{jk}\,\omega_{\mathrm{rand}}^2\tau_{\mathrm{rand}}$$

$$\Delta' = (\mathbb{T}_{20}^{g}|\hat{\Gamma}_{\mathrm{DD\times CSA}}^{\theta} + \hat{\Gamma}_{\mathrm{rand}}^{\theta}|\mathbb{T}_{10}^{g}) = -\frac{3\sqrt{3}}{10}\omega_0 b_{jk} \left(\delta_j^{\mathrm{CSA}} + \delta_k^{\mathrm{CSA}}\right) \frac{\tau_\perp}{1+\tau_\perp^2\omega_0^2} - \frac{(2+\kappa_{jk})}{\sqrt{3}}\omega_0\beta_\theta\,\omega_{\mathrm{rand}}^2\tau_{\mathrm{rand}}$$

$\lambda^{(2)}$ are equal to the non-zero eigenvalues after a change of sign, and correspond to the relaxation rate constants for the zero-quantum Liouvillian eigenoperators.

Using eq. (41), the polarization moment trajectories generally take a biexponential form and may be written:

$$\begin{aligned} \rho_{\ell 0}^{g}(\tau) &= (\mathbb{T}_{\ell 0}^{g}|\mathbf{S}\exp\{\mathbf{\Lambda}\tau\}\,\mathbf{S}^{-1}|\rho_{\mathrm{inv}}) \\ &= g_{\ell 0}^{g}\exp\{-\lambda^{(1)}\tau\} + h_{\ell 0}^{g}\exp\{-\lambda^{(2)}\tau\} + \rho_{\ell 0}^{g}(\mathrm{eq}). \end{aligned} \tag{44}$$

The coefficients $g_{\ell 0}^{g}$, $h_{\ell 0}^{g}$ and $\rho_{\ell 0}^{g}(\mathrm{eq})$ are given in table V for $\ell = 1$ and $\ell = 2$. From eq. (44), the polarization moments become equal to $\rho_{\ell 0}^{g}$ at equilibrium; i.e. at large τ (see table V).

Figure 10 compares numerical and analytical polarization moment trajectories for the parameters given in table II. The polarization moments are provided relative to the rank-1 polarization moment in thermal equilibrium, which is given through eq. (36) by,

$$\rho_{10}^{g}(\mathrm{eq}) = -\frac{1}{2\sqrt{2}}\omega_0\beta_\theta \tag{45}$$

The agreement is good. Cross-correlated DD-CSA relaxation induces the conversion of rank-1 polarization into rank-2 polarization, induced by the off-diagonal elements of the relaxation matrices shown in figure 9(c,e).

TABLE V. Rate constants $\lambda^{(1)}$ and $\lambda^{(2)}$, elements of $\mathbf{S}$, and coefficients $g^g_{\ell 0}$, $h^g_{\ell 0}$ and $k^g_{\ell 0}$ for $\ell = 1$ and $\ell = 2$.

$$\lambda^{(1)} = \frac{1}{2}\Big(\lambda_{10} + \lambda_{20} + \sqrt{4\Delta\Delta' + (\lambda_{10} - \lambda_{20})^2}\Big)$$

$$\lambda^{(2)} = \frac{1}{2}\Big(\lambda_{10} + \lambda_{20} - \sqrt{4\Delta\Delta' + (\lambda_{10} - \lambda_{20})^2}\Big)$$

$$S_{11} = \frac{\lambda_{10}\lambda_{20} - \Delta\Delta'}{\lambda_{10}\theta_{20} + \theta_{10}\Delta'}$$

$$S_{21} = \frac{\lambda_{20}\theta_{10} + \theta_{20}\Delta}{\lambda_{10}\theta_{20} + \theta_{10}\Delta'}$$

$$S_{22} = -\frac{1}{2\Delta'}\Big(\lambda_{10} - \lambda_{20} + \sqrt{4\Delta\Delta' + (\lambda_{10} - \lambda_{20})^2}\Big)$$

$$S_{23} = -\frac{1}{2\Delta'}\Big(\lambda_{10} - \lambda_{20} - \sqrt{4\Delta\Delta' + (\lambda_{10} - \lambda_{20})^2}\Big)$$

$$g^g_{10} = \frac{S_{22}}{2\,(S_{11}S_{22} - S_{11}S_{23})}\left(\frac{S_{11}\beta_\theta\omega_0}{\sqrt{2}} - S_{21} + S_{23}\right)$$

$$g^g_{20} = \frac{1}{2\,(S_{11}S_{22} - S_{11}S_{23})}\left(\frac{S_{11}\beta_\theta\omega_0}{\sqrt{2}} - S_{21} + S_{23}\right)$$

$$h^g_{10} = -\frac{S_{23}}{2\,(S_{11}S_{22} - S_{11}S_{23})}\left(\frac{S_{11}\beta_\theta\omega_0}{\sqrt{2}} - S_{21} + S_{23}\right)$$

$$h^g_{20} = -\frac{1}{2\,(S_{11}S_{22} - S_{11}S_{23})}\left(\frac{S_{11}\beta_\theta\omega_0}{\sqrt{2}} - S_{21} - S_{22}\right)$$

$$\rho^g_{10}(\mathrm{eq}) = -\frac{1}{2\sqrt{2}}\omega_0\beta_\theta$$

$$\rho^g_{20}(\mathrm{eq}) = 0$$

2. Observable coherences and peak amplitudes

In the inversion-recovery pulse sequence shown in figure 2, a pulse of flip angle β is applied after the evolution interval τ, and induces (-1)-quantum coherences which are detected in the subsequent interval. As described in our previous article [1], the operators representing the observable (-1)-quantum coherences are given in the near-equivalence limit by,

$$Q_+ = |T_0\rangle\langle T_{+1}|, \tag{46}$$

and,

$$Q_- = |T_{-1}\rangle\langle T_0|, \tag{47}$$

which are associated with the narrow and broad spectral peaks, respectively (see fig. 5).

From eq. (38), the peak amplitudes for an inversion-recovery experiment with flip angle β and evolution interval τ are given in terms of the polarization moments $\rho_{\ell 0}(\tau)$ by,

$$a_\pm(\beta,\tau) = \frac{1}{2}i\,\big(I^-|Q_\pm\big)\sum_\ell \big(Q_\pm|\hat{R}_0(\beta)|\mathbb{T}_{\ell 0}\big)\rho_{\ell 0}(\tau). \tag{48}$$

The complex pre-factor is required to describe quadrature detection [40]. In general, these equations predict a bi-exponential recovery of both spectral peak amplitudes, with exponential rate constants equal to $\lambda^{(1)}$ and $\lambda^{(2)}$:

$$\begin{aligned} a_\pm(\beta,\tau) = \frac{1}{2\sqrt{2}}\big\{&(\rho^g_{10}(\mathrm{eq}) \pm \sqrt{3}\,\rho^g_{20}(\mathrm{eq})\cos\beta)\sin\beta \\ &+ (g^g_{10} \pm \sqrt{3}\,g^g_{20}\cos\beta)\sin\beta\,\exp(-\lambda^{(1)}\tau) \\ &+ (h^g_{10} \pm \sqrt{3}\,h^g_{20}\cos\beta)\sin\beta\,\exp(-\lambda^{(2)}\tau)\big\} \end{aligned} \tag{49}$$

The terms $g^g_{\ell 0}$, $h^g_{\ell 0}$, $\rho^g_{\ell 0}(\mathrm{eq})$, and the rate constants $\lambda^{(1)}$ and $\lambda^{(2)}$, are given in table V.

A comparison of the experimental and analytical peak amplitudes for an inversion-recovery experiments with flip angles $\beta = 90°, 50°$ and $10°$ is shown in figure 6. The agreement is excellent.

Figure 4 shows several series of simulated spectra, for inversion-recovery experiments with different values of flip angle β, as a function of evolution interval τ. The good agreement of the simulated spectra (right) with the experimental spectra (left) is gratifying.

3. Population dynamics

We now consider the dynamics of the spin state populations under the inversion-recovery procedure. Consider a spin state $|r\rangle$. The population of $|r\rangle$ at a time τ after the inversion pulse may be expressed in terms of the polarization moments as follows:

$$\begin{aligned} p_r(\tau) &= \langle r|\rho(\tau)|r\rangle \\ &= \sum_{\ell=0}^{2}\langle r|\mathbb{T}_{\ell 0}|r\rangle\rho_{\ell 0}(\tau). \end{aligned} \tag{50}$$

The singlet and triplet populations are therefore given in terms of the polarization moments by the following expressions:

$$\begin{aligned} \Delta p^S_0 &= -\frac{\sqrt{3}}{2}\rho^g_{00}(\tau) \\ \Delta p^T_{+1} &= +\frac{1}{2\sqrt{3}}\rho^g_{00}(\tau) + \frac{1}{\sqrt{2}}\rho^g_{10}(\tau) + \frac{1}{\sqrt{6}}\rho^g_{20}(\tau) \\ \Delta p^T_0 &= +\frac{1}{2\sqrt{3}}\rho^g_{00}(\tau) - \frac{2}{\sqrt{6}}\rho^g_{20}(\tau) \\ \Delta p^T_{-1} &= +\frac{1}{2\sqrt{3}}\rho^g_{00}(\tau) - \frac{1}{\sqrt{2}}\rho^g_{10}(\tau) + \frac{1}{\sqrt{6}}\rho^g_{20}(\tau). \end{aligned} \tag{51}$$

where the deviation of a state population from the mean is denoted as follows:

$$\Delta p_r = p_r - \frac{1}{4}. \tag{52}$$

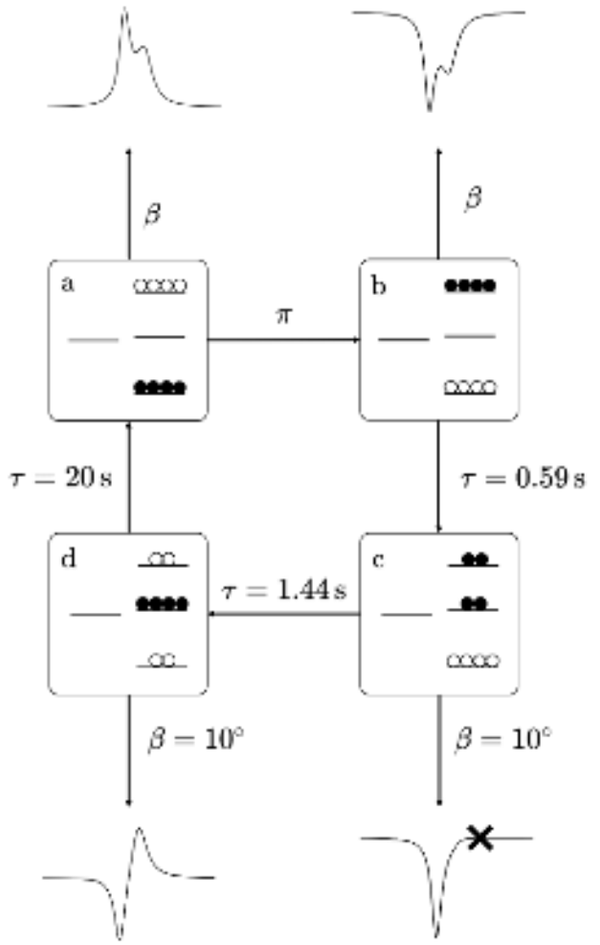

FIG. 11. Energy level diagram illustrating the population dynamics during the τ interval of an inversion-recovery experiment, and how that describes the behaviour of the peaks in the spectrum. All populations are described as deviations from a state with equal populations: Filled balls represent positive population deviations, while empty balls represent negative population deviations. a) Spin state populations at thermal equilibrium. b) A π-pulse inverts populations, and a pulse with arbitrary β gives an inverted spectrum. c) After a delay $\tau = 0.59$ s and a 10°-pulse, the peak associated with the Q_- coherence vanishes. d) After a delay $\tau = 1.44$ s the rank-1 polarization moment $\rho^g_{10}(\tau)$ vanishes, and peaks with amplitude of opposite sign are observed. A further delay restores thermal equilibrium.

From the trajectories in section IV E 1, the populations of the states $|T_{+1}\rangle$ and $|T_0\rangle$ become equal after a time interval $\tau = 0.59\,\mathrm{s}$. As a result, the broad spectral peak vanishes for this value of τ, when a small flip angle β is used. This effect is evident by comparing figures 6 and 10.

Using the polarization moment trajectories with eq. 51 and peak amplitudes, the movement of populations between the states in the interval τ of the inversion-recovery experiment, and the spectra obtained by taking the Fourier transform of the signal induced by the final pulse, may be invoked. These are sketched in figure 11.

F. Relaxation Field-Dependence

1. Longitudinal relaxation

From eq. (49), the total signal amplitude, for an inversion-recovery experiment with flip angle β, is given as a function of τ by,

$$\begin{aligned} a(\beta,\tau) &= a_+(\beta,\tau) + a_-(\beta,\tau) \\ &= \frac{1}{\sqrt{2}}\sin\beta\big\{\rho^g_{10}(\mathrm{eq}) + g^g_{10}\,\exp(-\lambda^{(1)}\tau) \\ &\quad + h^g_{10}\,\exp(-\lambda^{(2)}\tau)\big\}. \end{aligned} \tag{53}$$

For long τ, the above expression tends to a value proportional to thermal equilibrium magnetization:

$$\lim_{\tau\to\infty} a(\beta,\tau) = \frac{1}{\sqrt{2}}\rho^g_{10}(\mathrm{eq})\sin\beta. \tag{54}$$

In general, eq. (53) describes a bi-exponential recovery to equilibrium.

Since the recovery is bi-exponential, it is not possible to give a theoretical expression for the single parameter T_1 over the full range of magnetic fields. As such, the function in eq. (2) was fitted to recovery curves calculated via eq. (49) and T_1 extrapolated. These theoretical values of T_1 are plotted in fig. 7a. There is some discrepancy, potentially due to population exchanges taking place during the shuttling process, which takes a finite amount of time.

2. Singlet relaxation

The theory given above predicts a single-exponential decay of the polarization moment $\rho^g_{00}(\tau)$, according to

$$\rho^g_{00}(\tau) = \rho^g_{00}(0)e^{-\lambda^g_{00}\tau} \tag{55}$$

As shown in table VI, the intra-pair dipole-dipole mechanism and the CSA-DD cross-correlation terms do not contribute to the singlet relaxation. The theoretical decay rate constant for singlet order is therefore given by,

$$\begin{aligned} \lambda^g_{00} &= \lambda^{\mathrm{CSA}}_{00} + \lambda^{\mathrm{rand}}_{00} \\ &= \frac{1}{3}\omega_0^2(\Delta\delta_{\mathrm{CSA}})^2\tau_\perp + 2\,(1-\kappa_{jk})\,\omega^2_{\mathrm{rand}}\tau_{\mathrm{rand}}, \end{aligned} \tag{56}$$

where $\Delta\delta_{\mathrm{CSA}}$ is the CSA difference parameter.

For simplicity, we assume uncorrelated fields and arbitrarily set $\kappa_{jk} = 0$. Then, the product of the mean-squared random-field amplitude and the random field correlation time, $\omega^2_{\mathrm{rand}}\tau_{\mathrm{rand}}$, may be estimated from the inversion-recovery data at 9.4 T for $\beta = 10°, 50°, 90°$ flip-angle experiments and $\Delta\delta_{\mathrm{CSA}}$ in turn by fitting the experimental field-dependence of the singlet relaxation rate

TABLE VI. Analytical relaxation rate constants for singlet order in the extreme-narrowing limit and utilising the high-temperature approximation. The chemical shift difference is given by the parameter, $\Delta\delta_{\mathrm{CSA}} = \delta_j^{\mathrm{CSA}} - \delta_k^{\mathrm{CSA}}$.

$$\lambda_{00}^{\mathrm{DD}} \simeq -(\mathbb{T}_{00}^{g}|\hat{\Gamma}_{\mathrm{DD}}^{\theta}|\mathbb{T}_{00}^{g}) = 0$$

$$\lambda_{00}^{\mathrm{CSA}} \simeq -(\mathbb{T}_{00}^{g}|\hat{\Gamma}_{\mathrm{CSA}}^{\theta}|\mathbb{T}_{00}^{g}) = \frac{1}{3}\omega_0^2(\Delta\delta_{\mathrm{CSA}})^2\tau_{\perp}$$

$$\lambda_{00}^{\mathrm{DD\times CSA}} \simeq -(\mathbb{T}_{00}^{g}|\hat{\Gamma}_{\mathrm{DD\times CSA}}^{\theta}|\mathbb{T}_{00}^{g}) = 0.$$

$$\lambda_{00}^{\mathrm{rand}} \simeq -(\mathbb{T}_{00}^{g}|\hat{\Gamma}_{\mathrm{rand}}^{\theta}|\mathbb{T}_{00}^{g}) = 2\,(1-\kappa_{jk})\,\omega_{\mathrm{rand}}^2\tau_{\mathrm{rand}}$$

constant, shown in figure 7b. This leads to the best-fit parameter set given in table II.

The theoretical singlet order decay is compared to the experimental data in figure 8. The agreement is excellent. The theoretical field-dependence of the singlet order decay rate constant is compared to the experimental data in figure 7b. The agreement is good, except at low magnetic field, where an additional contribution to the singlet relaxation rate is evident. This indicates the presence of additional mechanisms with a longer correlation time, such as paramagnetic relaxation by dissolved oxygen [56, 57].

The best-fit value for the CSA difference parameter $\Delta\delta_{\mathrm{CSA}} \simeq 13.3$ ppm is much larger than an estimate provided by DFT (density functional theory) calculations for the equilibrium molecular geometry. This indicates that less symmetrical non-equilibrium geometries are important participants in singlet order relaxation. A similar conclusion was drawn from a study of nuclear singlet relaxation in different molecular systems [58].

V. DISCUSSION AND CONCLUSIONS

In this paper, and the previous one [1], we have presented a comprehensive study of the nuclear spin dynamics in a system containing an isolated spin-1/2 pair, and which exhibits anisotropic rotational diffusion and strong cross-correlation effects. The spin pair is almost magnetically equivalent, so that the Hamiltonian eigenstates are given by the singlet and triplet nuclear spin states, to a good approximation. As described in the previous paper [1], the strong cross-correlation of the dipole-dipole and chemical shift anisotropy interactions leads to a strong difference between the widths of the two main spectral peaks.

In this paper, we show how the cross-correlation leads to a strong difference between the trajectories of the two peaks in an inversion-recovery experiment with a small flip angle for the final read-out pulse. The broad peak recovers from inversion much more rapidly than the narrow peak in these experiments. This effect is well-explained by a theoretical description using a Lindbladian formulation of the relaxation superoperator which takes into account the finite temperature of the molecular environment.

Singlet NMR experiments reveal the existence of very long-lived nuclear singlet order, with a time constant ratio T_S/T_1 exceeding 100 over a range of magnetic fields. The experimental results are explained well by a theoretical model including relaxation by chemical shift anisotropy, dipole-dipole coupling, and their cross-correlation. A full description also requires the inclusion of fluctuating magnetic fields at the sites of the nuclear spins, and in our treatment, uncorrelated fields are assumed for simplicity.

SUPPLEMENTARY MATERIAL

The supplementary material contains experimental parameters, simulation details for the numerical and analytical analysis. A Mathematica notebook is available on request.

ACKNOWLEDGEMENTS

The authors thank Alexey Kiryutin for sharing shuttle-system designs. This research was supported by the European Research Council (grant 786707-FunMagResBeacons) and EPSRC (grants EP/V055593/1 and EP/P030491/1).

DATA AVAILABILITY

A Mathematica notebook is available upon request.

[1] J. W. Whipham, G. A. I. Moustafa, M. Sabba, W. Gong, C. Bengs, and M. H. Levitt, Cross-correlation effects in the solution NMR spectra of near-equivalent spin-1/2

pairs, J. Chem. Phys. **157**, 104112 (2022).
[2] M. C. D. Tayler and M. H. Levitt, Singlet nuclear magnetic resonance of nearly-equivalent spins, Phys. Chem. Chem. Phys. **13**, 5556 (2011).
[3] H. M. McConnell, Effect of Anisotropic Hyperfine Interactions on Paramagnetic Relaxation in Liquids, J. Chem. Phys. **25**, 709 (1956).
[4] H. Shimizu, Theory of the Dependence of Nuclear Magnetic Relaxation on the Absolute Sign of Spin—Spin Coupling Constant, J. Chem. Phys. **40**, 3357 (1964).
[5] L. G. Werbelow and D. M. Grant, Intramolecular Dipolar Relaxation in Multispin Systems, Adv. Magn. Reson. **9**, 189 (1977).
[6] M. Goldman, Interference effects in the relaxation of a pair of unlike spin-1/2 nuclei, J. Magn. Reson. **60**, 437 (1984).
[7] L. Di Bari, J. Kowalewski, and G. Bodenhausen, Magnetization transfer modes in scalar-coupled spin systems investigated by selective two-dimensional nuclear magnetic resonance exchange experiments, J. Chem. Phys. **93**, 7698 (1990).
[8] A. Kumar, R. Christy Rani Grace, and P. K. Madhu, Cross-correlations in NMR, Prog. Nucl. Mag. Res. Sp. **37**, 191 (2000).
[9] P. K. Madhu, P. K. Mandal, and N. Müller, Cross-Correlation Effects Involving Curie Spin Relaxation in Methyl Groups, J. Magn. Reson. **155**, 29 (2002).
[10] J. Kowalewski and L. Mäler, *Nuclear Spin Relaxation in Liquids Theory, Experiments, and Applications*, 2nd ed. (CRC Press, Taylor & Francis Group, Boca Raton, FL, 2018).
[11] L. G. Werbelow and D. M. Grant, Carbon-13 relaxation in multispin systems of the type AX n, The Journal of Chemical Physics **63**, 544 (1975).
[12] K. Dorai and A. Kumar, Fluorine chemical shift tensors in substituted fluorobenzenes using cross correlations in NMR relaxation, Chemical Physics Letters **335**, 176 (2001).
[13] A. Kumar and P. K. Madhu, Cross-correlations in multispin relaxation, Concepts Magn. Reson. **8**, 139 (1996).
[14] C. Dalvit and G. Bodenhausen, Proton chemical shift anisotropy: Detection of cross-correlation with dipole-dipole interactions by double-quantum filtered two-dimensional NMR exchange spectroscopy, Chemical Physics Letters **161**, 554 (1989).
[15] G. Pileio, Singlet NMR methodology in two-spin-1/2 systems, Prog. Nucl. Mag. Res. Sp. **98–99**, 1 (2017).
[16] M. H. Levitt, Long live the singlet state!, J. Magn. Reson. **306**, 69 (2019).
[17] G. Stevanato, J. T. Hill-Cousins, P. Håkansson, S. S. Roy, L. J. Brown, R. C. D. Brown, G. Pileio, and M. H. Levitt, A Nuclear Singlet Lifetime of More than One Hour in Room-Temperature Solution, Angew. Chem. Int. Ed. **54**, 3740 (2015).
[18] A. Moysiadi, F. Giustiniano, A. M. R. Hall, T. A. A. Cartlidge, L. J. Brown, and G. Pileio, Nuclear Spin Relaxation of Longitudinal and Singlet Order in Liquid-CO2 Solutions, Front. Chem. **9**, 668044 (2021).
[19] R. K. Wangsness and F. Bloch, The Dynamical Theory of Nuclear Induction, Phys. Rev. **89**, 728 (1953).
[20] A. Redfield, The Theory of Relaxation Processes, Adv. Magn. Reson. **1**, 1 (1965).
[21] A. Abragam, *The Principles of Nuclear Magnetism*, repr ed., International Series of Monographs on Physics No. 32 (Oxford Univ. Pr, Oxford, 2011).
[22] R. R. Ernst, G. Bodenhausen, and A. Wokaun, *Principles of Nuclear Magnetic Resonance in One and Two Dimensions*, The International Series of Monographs on Chemistry No. 14 (Clarendon press, Oxford, 1992).
[23] C. Bengs and M. H. Levitt, A master equation for spin systems far from equilibrium, J. Magn. Reson. **310**, 106645 (2020).
[24] M. H. Levitt and C. Bengs, Hyperpolarization and the physical boundary of Liouville space, Magn. Reson. **2**, 395 (2021).
[25] G. Lindblad, On the generators of quantum dynamical semigroups, Commun. Math. Phys. **48**, 119 (1976).
[26] A. Karabanov, G. Kwiatkowski, and W. Köckenberger, Spin dynamic simulations of solid effect DNP: The role of the relaxation superoperator, Molecular Physics **112**, 1838 (2014).
[27] H.-P. Breuer and F. Petruccione, *The Theory of Open Quantum Systems* (Clarendon, Oxford, 2007).
[28] A. S. Kiryutin, A. N. Pravdivtsev, K. L. Ivanov, Y. A. Grishin, H.-M. Vieth, and A. V. Yurkovskaya, A fast field-cycling device for high-resolution NMR: Design and application to spin relaxation and hyperpolarization experiments, Journal of Magnetic Resonance **263**, 79 (2016).
[29] I. V. Zhukov, A. S. Kiryutin, A. V. Yurkovskaya, Y. A. Grishin, H.-M. Vieth, and K. L. Ivanov, Field-cycling NMR experiments in an ultra-wide magnetic field range: Relaxation and coherent polarization transfer, Phys. Chem. Chem. Phys. **20**, 12396 (2018).
[30] M. H. Levitt, Composite pulses, Progress in Nuclear Magnetic Resonance Spectroscopy **18**, 61 (1986).
[31] B. A. Rodin, K. F. Sheberstov, A. S. Kiryutin, L. J. Brown, R. C. D. Brown, M. Sabba, M. H. Levitt, A. V. Yurkovskaya, and K. L. Ivanov, Fast destruction of singlet order in NMR experiments, J. Chem. Phys. **151**, 234203 (2019).
[32] M. C. D. Tayler and M. H. Levitt, Accessing Long-Lived Nuclear Spin Order by Isotope-Induced Symmetry Breaking, J. Am. Chem. Soc. **135**, 2120 (2013).
[33] M. H. Levitt, The Signs of Frequencies and Phases in NMR, J. Magn. Reson. **126**, 164 (1997).
[34] C.-L. Teng, H. Hong, S. Kiihne, and R. G. Bryant, Molecular Oxygen Spin–Lattice Relaxation in Solutions Measured by Proton Magnetic Relaxation Dispersion, Journal of Magnetic Resonance **148**, 31 (2001).
[35] C. Bengs and M. H. Levitt, SpinDynamica: Symbolic and numerical magnetic resonance in a Mathematica environment, Magn. Reson. Chem. **56**, 374 (2018).
[36] M. Carravetta and M. H. Levitt, Theory of long-lived nuclear spin states in solution nuclear magnetic resonance. I. Singlet states in low magnetic field, J. Chem. Phys. **122**, 214505 (2005).
[37] P. S. Hubbard, Theory of Nuclear Magnetic Relaxation by Spin-Rotational Interactions in Liquids, Phys. Rev. **131**, 1155 (1963).
[38] C. Wang, Anisotropic-rotational diffusion model calculation of T1 due to spin-rotation interaction in liquids, J. Magn. Reson. **9**, 75 (1973).
[39] M. J. Frisch, G. W. Trucks, H. B. Schlegel, G. E. Scuseria, M. A. Robb, J. R. Cheeseman, G. Scalmani, V. Barone, G. A. Petersson, H. Nakatsuji, X. Li, M. Caricato, A. V. Marenich, J. Bloino, B. G. Janesko, R. Gomperts, B. Mennucci, H. P. Hratchian, J. V. Or-

tiz, A. F. Izmaylov, J. L. Sonnenberg, D. Williams-Young, F. Ding, F. Lipparini, F. Egidi, J. Goings, B. Peng, A. Petrone, T. Henderson, D. Ranasinghe, V. G. Zakrzewski, J. Gao, N. Rega, G. Zheng, W. Liang, M. Hada, M. Ehara, K. Toyota, R. Fukuda, J. Hasegawa, M. Ishida, T. Nakajima, Y. Honda, O. Kitao, H. Nakai, T. Vreven, K. Throssell, J. A. Montgomery, Jr., J. E. Peralta, F. Ogliaro, M. J. Bearpark, J. J. Heyd, E. N. Brothers, K. N. Kudin, V. N. Staroverov, T. A. Keith, R. Kobayashi, J. Normand, K. Raghavachari, A. P. Rendell, J. C. Burant, S. S. Iyengar, J. Tomasi, M. Cossi, J. M. Millam, M. Klene, C. Adamo, R. Cammi, J. W. Ochterski, R. L. Martin, K. Morokuma, O. Farkas, J. B. Foresman, and D. J. Fox, Gaussian 09 (2016), Gaussian, Inc. Wallingford CT.

[40] M. H. Levitt, *Spin Dynamics: Basics of Nuclear Magnetic Resonance*, 2nd ed. (John Wiley & Sons, Chichester, England ; Hoboken, NJ, 2008).

[41] M. Sabba, N. Wili, C. Bengs, J. W. Whipham, L. J. Brown, and M. H. Levitt, Symmetry-based singlet–triplet excitation in solution nuclear magnetic resonance, J. Chem. Phys. **157**, 134302 (2022).

[42] A. G. Redfield, On the Theory of Relaxation Processes, IBM J. Res. Dev. **1**, 19 (1957).

[43] G. Pileio, Relaxation theory of nuclear singlet states in two spin-1/2 systems, Prog. Nucl. Mag. Res. Sp. **56**, 217 (2010).

[44] R. Dümcke and H. Spohn, The proper form of the generator in the weak coupling limit, Z Physik B **34**, 419 (1979).

[45] H. Spohn, Kinetic equations from Hamiltonian dynamics: Markovian limits, Rev. Mod. Phys. **52**, 569 (1980).

[46] A. Suárez, R. Silbey, and I. Oppenheim, Memory effects in the relaxation of quantum open systems, J. Chem. Phys. **97**, 5101 (1992).

[47] P. Pechukas, Reduced Dynamics Need Not Be Completely Positive, Phys. Rev. Lett. **73**, 1060 (1994).

[48] D. Manzano, A short introduction to the Lindblad master equation, AIP Adv. **10**, 025106 (2020).

[49] G. Pileio, M. Carravetta, E. Hughes, and M. H. Levitt, The Long-Lived Nuclear Singlet State of 15N-Nitrous Oxide in Solution, J. Am. Chem. Soc. **130**, 12582 (2008).

[50] B. Kharkov, X. Duan, J. Rantaharju, M. Sabba, M. H. Levitt, J. W. Canary, and A. Jerschow, Weak nuclear spin singlet relaxation mechanisms revealed by experiment and computation, Phys. Chem. Chem. Phys. **24**, 7531 (2022).

[51] D. E. Korenchan, J. Lu, M. Sabba, L. Dagys, L. J. Brown, M. H. Levitt, and A. Jerschow, ^{31} P spin–lattice and singlet order relaxation mechanisms in pyrophosphate studied by isotopic substitution, field shuttling NMR, and molecular dynamics simulation, Phys. Chem. Chem. Phys. **24**, 24238 (2022).

[52] G. Pileio, Singlet state relaxation via intermolecular dipolar coupling, J. Chem. Phys. **134**, 214505 (2011).

[53] G. Schaller, *Open Quantum Systems Far from Equilibrium*, Lecture Notes in Physics, Vol. 881 (Springer International Publishing, Cham, 2014).

[54] C. Bengs, L. Dagys, G. A. I. Moustafa, J. W. Whipham, M. Sabba, A. S. Kiryutin, K. L. Ivanov, and M. H. Levitt, Nuclear singlet relaxation by chemical exchange, J. Chem. Phys. **155**, 124311 (2021).

[55] M. Auzinsh, D. Budker, and S. Rochester, *Optically Polarized Atoms: Understanding Light-Atom Interactions* (Oxford University Press, Oxford, New York, 2014).

[56] M. C. D. Tayler and M. H. Levitt, Paramagnetic relaxation of nuclear singlet states, Phys. Chem. Chem. Phys. **13**, 9128 (2011).

[57] B. Erriah and S. J. Elliott, Experimental evidence for the role of paramagnetic oxygen concentration on the decay of long-lived nuclear spin order, RSC Adv. **9**, 23418 (2019).

[58] G. Pileio, J. T. Hill-Cousins, S. Mitchell, I. Kuprov, L. J. Brown, R. C. D. Brown, and M. H. Levitt, Long-Lived Nuclear Singlet Order in Near-Equivalent ^{13} C Spin Pairs, J. Am. Chem. Soc. **134**, 17494 (2012).